Available online at www.sciencedirect.com
SCIENCE DIRECT®
Biomaterials 27 (2006) 4477–4483
Biomaterials
www.elsevier.com/locate/biomaterials

PEGylated albumin-heme as an oxygen-carrying plasma expander: Exchange transfusion into acute anemia rat model

Yubin Huang[a], Teruyuki Komatsu[a], Hisashi Yamamoto[b,c], Hirohisa Horinouchi[c], Koichi Kobayashi[c], Eishun Tsuchida[a,*]

[a]*Advanced Research Institute for Science and Engineering, Waseda University, 3-4-1 Okubo, Shinjuku-ku, Tokyo 169 8555, Japan*
[b]*Pharmaceutical Research Center, NIPRO Corp., 3023 Noji-cho, Kusatsu-shi, Shiga 525 0055, Japan*
[c]*Department of General Thoracic Surgery, School of Medicine, Keio University, 35 Shinanomachi, Shinjuku-ku, Tokyo 160 8582, Japan*

Received 11 January 2006; accepted 5 April 2006
Available online 4 May 2006

Abstract

Poly(ethylene glycol) (PEG) conjugated recombinant human serum albumin (HSA) incorporating the synthetic iron-porphyrin (FeP) [PEGylated albumin-heme, PEG(HSA–FeP)] is a unique albumin-based oxygen carrier as a red blood cell (RBC) substitute. The physiological responses to an exchange transfusion with PEG(HSA–FeP) into an acute anemia rat model were investigated. After a 65% isovolemic hemodilution with HSA, a 30% volume of the circulatory blood was withdrawn, affording a hemorrhaged state. The circulation parameters, blood parameters, renal cortical oxygen partial pressure [PtO_2(R)], and muscle tissue oxygen partial pressure [PtO_2(M)] were continuously monitored. The intravenous infusion of PEG(HSA–FeP) restored the reduced levels of the mean arterial pressure, heart rate, respiration rate, mixed venous PO_2, and arterial PCO_2. The increased arterial PO_2 and pH also returned to their basal values. These effects were almost to the same extent as those observed after the administration of the RBC suspension. The relatively low recovery in PtO_2(R) and PtO_2(M) might be due to the Langmuir-type oxygen binding profile of PEG(HSA–FeP) (Hill coefficient: 1.0). All the animals survived during the experiments. In contrast, those injected with HSA died within 41 min. The PEG(HSA–FeP) solution is an oxygen-carrying plasma expander which can be used as a resuscitative fluid for hemorrhagic shock.

Keywords: Albumin; Biomimetic material; Blood; In vivo test; Oxygenation; Poly(ethylene glycol)

1. Introduction

Human hemoglobin (Hb)-based oxygen carriers as a blood replacement composition have been vigorously developed in the past decade [1–3], e.g., polymerized Hb [4], polymer-conjugated Hb [5], and phospholipid vesicle encapsulated Hb [6,7]. Some of them have already been used in clinical Phase II/III trials. The most superior property of these materials is certainly "no blood type". One can administer these materials into patients who need a blood transfusion without cross matching and typing before use. This saves time and facilities, allowing instant transfusion, which is tremendously useful in an emergency. On the other hand, the largest concern of the Hb-products is the source of the human Hb, which is regulated by the availability of donated human blood.

Based on this background, poly(ethylene glycol) (PEG) conjugated human serum albumin (HSA) incorporating 2-[8-{*N*-(2-methylimidazolyl)}octanoyloxymethyl]-5,10,15,20-tetrakis{α,α,α,α-*o*-(1-methylcyclohexanamido)phenyl}porphinatoiron(II) (FeP, Chart 1) [PEGylated albumin-heme, PEG(HSA–FeP)] has been developed as a unique albumin-based oxygen carrier [8]. Recombinant HSA is now manufactured on an industrial scale (one million vials per year) [9] and the batch production of the synthetic FeP has also been established [10]. The oxygen binding affinity (oxygen pressure where 50% of heme is oxygenated) of PEG(HSA–FeP) (P_{50}) was adjusted to 32 Torr (at 37 °C) that is similar to the 28 Torr of human RBC, and the solution properties are almost the same as those of HSA itself. The surface modification with PEG significantly improved not only the

*Corresponding author. Tel.: +81 3 5286 3120; fax: +81 3 3205 4740.
E-mail address: eishun@waseda.jp (E. Tsuchida).

0142-9612/$ - see front matter © 2006 Elsevier Ltd. All rights reserved.
doi:10.1016/j.biomaterials.2006.04.008

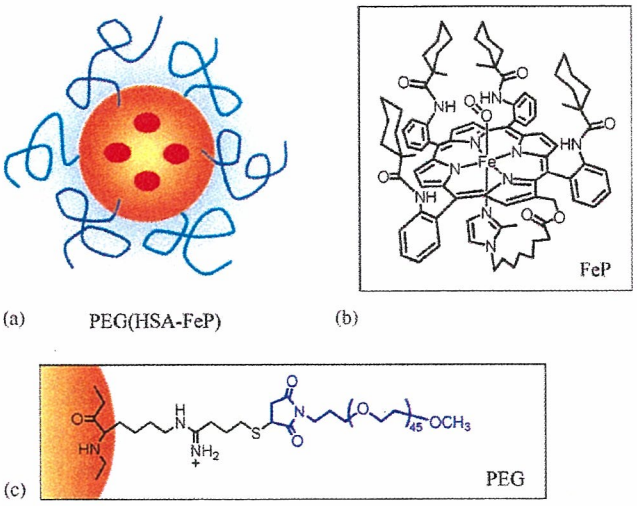

Chart 1. (a) Schematic illustration of PEGylated albumin-heme [PEG(HSA–FeP)], (b) chemical structure of FeP, and (c) binding form of PEG to the lysine group of HSA.

circulation lifetime of FeP in vivo, but also the stability of the oxygenated complex [8]. The PEG(HSA–FeP) solution would be of extreme medical importance as a new type of oxygen-carrying plasma expander.

We now report for the first time the systemic evaluations of the physiological responses to an exchange transfusion with PEG(HSA–FeP) into an acute anemia rat model. The animals were first placed in a 65 vol% hemodilution with HSA and then underwent a 30 vol% blood replacement with PEG(HSA–FeP). The circulation parameters, blood parameters, the oxygen deliveries to the renal cortex and the muscle tissue were monitored and compared to the HSA group and RBC group for 120 min after the infusion.

2. Materials and methods

2.1. Preparation of PEG(HSA–FeP) solution

The 5 g/dL HSA solution was prepared by dilution of recombinant HSA [Albrec®, 25 wt%, NIPRO Corp. (Osaka)] with a saline (Otsuka Pharmaceutical Co., Ltd.). The PEG(HSA–FeP) was prepared according to our previously reported procedure [8] (phosphate buffer saline solution, pH = 7.4, [HSA] = 5 g/dL, [FeP] = 3 mM (FeP/HSA = 4 mol/mol), Mw of PEG = 2333 Da, averaged number of PEG per HSA–FeP = 6, oxygen-binding affinity (P_{50}) = 32 Torr (37 °C), density = 1.01 g/cm^3, colloid osmotic pressure = 27 mmHg, viscosity = 1.14 cP).

2.2. Extreme hemodilution and exchange transfusion

The investigations were carried out with 15 male Wistar rats (288 ± 18 g). The methods of operation were described elsewhere in detail [11].

The animals were under an inhalation anesthesia with sevoflurane; its concentration was kept at 1.5% during the experiment. First, a 65% hemodilution was carried out using 5 g/dL HSA. The blood withdrawal via the common carotid artery (2 mL) and the HSA infusion from the femoral vein (2 mL) (each 1 mL/min) were repeated for eight cycles. After 10 min, a 30% volume of the circulatory blood was withdrawn, and the identical volume of PEG(HSA–FeP) was injected ($n = 5$) (1 mL/min). As negative or positive-control group, the 5 g/dL HSA solution (HSA group, $n = 5$) or the washed RBC suspension (RBC group, $n = 5$) was infused to the similarly operated rats in hemorrhage. The washed RBC suspension was prepared as follows. The fresh withdrawn whole rat blood in the heparinized tube was centrifuged and the plasma layer was discarded. The 5 g/dL HSA was added to the tube and centrifuged again. Then, the supernatant was discarded and 5 g/dL HSA was added to adjust the Hb concentration to 5 g/dL ([heme] = 3 mM).

The blood samples from the artery (0.3 mL) and vein (0.2 mL) were collected at the following seven time-points: (1) before the 65% hemodilution, (2) immediately after the hemodilution, (3) 10 min after the hemodiluation, (4) immediately after the 30% bleeding, (5) immediately after the sample infusion, (6) 60 min, and (7) 120 min after the infusion. Mean arterial pressure (MAP) and heart rate (HR) were recorded by a Polygraph System (NIHON KODEN LEG-1000 Ver. 01-02 or PEG-1000 Ver. 01-01) at the following eleven time-points; (1) before the 65% hemodilution, (2) immediately after the hemodilution, (3) 10 min after the hemodilution, (4) immediately after the 30% bleeding, (5) immediately after the sample infusion, (6) 5 min, (7) 15 min, (8) 30 min, (9) 60 min, (10) 90 min, and (11) 120 min after the sample infusion. Collected blood sample was applied to a blood gas system (Radio Meter Trading ABL555) to measure the oxygen pressure (PaO_2), carbon dioxide pressure ($PaCO_2$) and pH of the arterial blood, and the oxygen pressure (PvO_2) and lactate of the venous blood. Renal cortical oxygen partial pressure [PtO_2(R)] and muscle tissue oxygen partial pressure [PtO_2(M)] were monitored by a tissue oxygen pressure monitor (Inter Medical PO_2-100 DW) using a polarographic oxygen-electrode (Intermedical POE-10 N and POE-40PS) inserted into the left renal cortex and muscle in the abdomen.

The animals were sacrificed after the experiments by venesection. All animal handling and care were in accordance with the NIH guidelines. The protocol details were approved by the Animal Care and Use Committee of Keio University.

2.3. Statistical analysis

All data were represented by mean ± standard deviation (SD). Statistical analyses ware performed using the Tukey–Kramer multiple comparison test for three groups, and by repeated measures analysis of variance followed by paired t-test. The software used was a StatView (SAS Institute, Inc.). Values of $p < 0.05$ were considered significant.

3. Results

3.1. Survival time

The changes in the hematocrit (Hct) clearly demonstrated a good accordance with the 65% hemodilution and 30% shock resuscitation (Fig. 1(a)). Isovolemic hemodilution with HSA reduced the Hct to 13–15%; this value is below the threshold at which the organism becomes oxygen supply limited [12,13]. Under an extreme hemodilution, the effect of the RBC substitute is magnified upon introduction into the circulation.

The intravenous infusion of HSA did not make any improvement on the appearance of the animals. All the rats died within 41 min; the average survival time was 17.9 ± 14.0 min (Fig. 1(b)). In contrast, after the transfusion of PEG(HSA–FeP) or washed RBC, all the animals survived over 120 min. In the glass capillaries for the Hct determinations of the PEG(HSA–FeP) group, the supernatant after centrifugation (12 kG, 5 min) was colored red by the homogeneously dispersed sample. This indicates that PEG(HSA–FeP) has a good solubility with the blood components without aggregation.

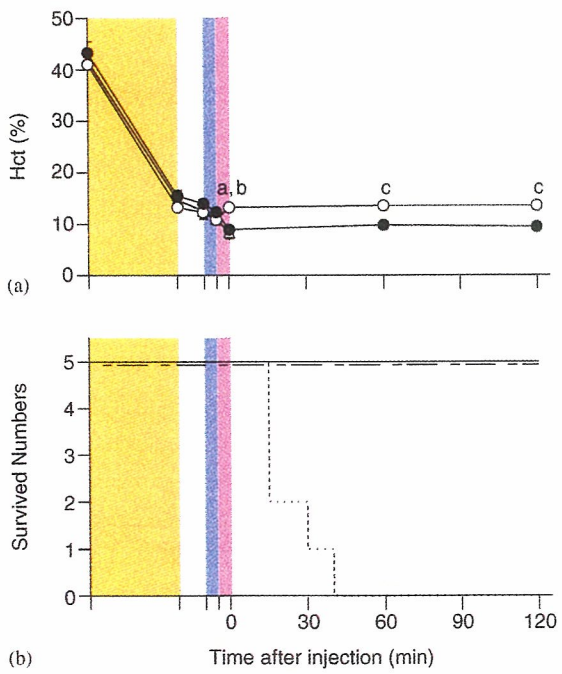

Fig. 1. Effect of PEG(HSA–FeP) solution on (a) Hct in anesthetized rats subjected to hemodilution and hemorrhage, and (b) the changes of their survived numbers. In (a), each value represents the mean ± SD of 5 rats [●; PEG(HSA–FeP) group, ○; RBC group, and △; HSA group]. $^{a}p<0.05$ versus HSA group (Tukey–Kramer test), $^{b}p<0.05$ versus PEG(HSA–FeP) group (Tukey–Kramer test), and $^{c}p<0.05$ versus PEG(HAS–FeP) group (unpaired t-test). In (b), solid line; PEG(HSA–FeP) group, broken and dotted line; RBC group, and dotted line; HSA group. The yellow, blue, and pink areas indicate the periods of 65% hemodilution, 30% bleeding, and sample infusion, respectively.

3.2. Circulation parameters (MAP, HR, and respiration rate)

The MAP decreased to 70–73 mmHg [72–74% of the basal value (b.v.)] after the 65% hemodilution, and further dropped to 28–29 mmHg (28–29% of the b.v.) by the 30% bleeding in all groups (Fig. 2(a)). The injection of PEG(HSA–FeP) or RBC significantly increased the lowered values to 70 or 73 mmHg, that corresponds to 85% or 98% of the levels before the bleedings. On the other hand, no recovery was observed in the HSA group.

The HR and respiration rate decreased to 332–356 beats/min (86–91% of the b.v.) and 51–57 time/min (80–93% of the b.v.) by the 30% bleeding (Fig. 2(b), (c)). Both parameters returned to their initial levels by the infusion of PEG(HSA–FeP). The degree of the recovery was almost the same as those of the RBC transfusion.

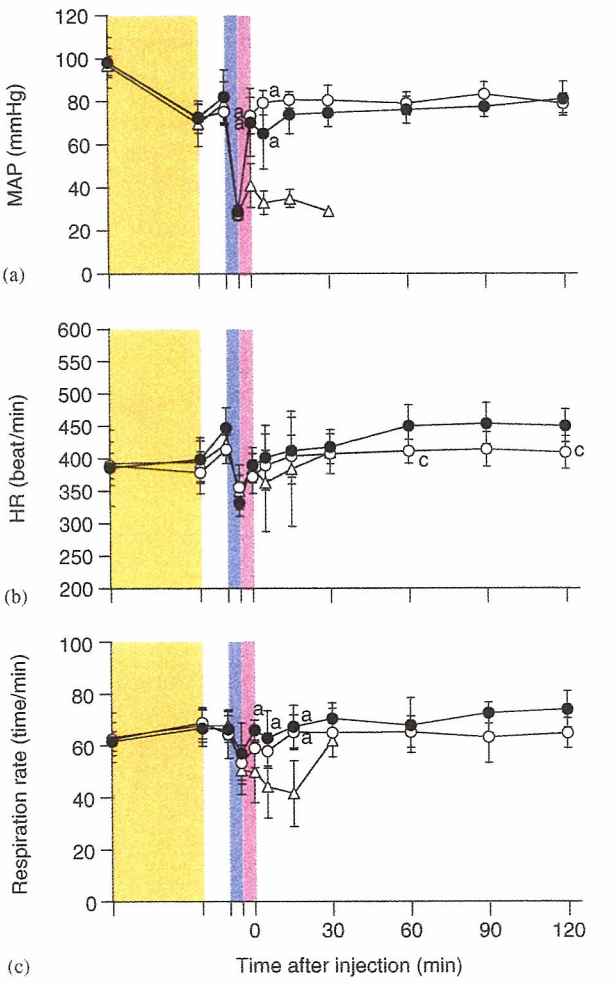

Fig. 2. Effect of PEG(HSA–FeP) solutions on (a) MAP, (b) HR, and (c) respiration rate in anesthetized rats subjected to hemodilution and hemorrhage. Each value represents the mean ± SD of 5 rats [●; PEG(HSA–FeP) group, ○; whole blood group, and △; HSA group]. The yellow, blue, and pink areas indicate the periods of 65% hemodilution, 30% bleeding, and sample infusion, respectively. $^{a}p<0.05$ versus HSA group (Tukey–Kramer test) and $^{c}p<0.05$ versus PEG(HAS–FeP) group (unpaired t-test).

3.3. Blood parameters [PaO_2, PvO_2, $PaCO_2$, and pH]

The PaO_2 increased to 96–118 mmHg (120–140% of the b.v.) after the 65% hemodilution, and became further elevated to 131–137 mmHg (156–167% of the b.v.) after the 30% bleeding (Fig. 3(a)). It was not changed by the injection of HSA, however, the administration of RBC immediately restored the PaO_2 to 97 mmHg (118% of the b.v.), and kept the level constant throughout the measurement. The injection of PEG(HSA–FeP) also showed a similar restoration like that of RBC.

The PvO_2 decreased to 32–35 mmHg (59–67% of the b.v.) after the 30% bleeding (Fig. 3(b)). Although the administration of HSA did not improve the low value, the infusion of PEG(HSA–FeP) or RBC increased the PvO_2 to 49 or 52 mmHg (91% or 95% of the the b.v.).

The $PaCO_2$ dropped to 23–26 mmHg (59–66% of the b.v.) after the 30% bleeding (Fig. 3(c)). The injection of HSA did not recover the low level, while the administration of PEG(HSA–FeP) or RBC increased the $PaCO_2$ to 31 mmHg, and it reached 35 mmHg after 1 h.

The pH of 7.43–7.45 was increased to 7.53–7.56 after the 30% bleeding. The administration of PEG(HSA–FeP) or RBC quickly decreased the high pH to the initial value before the hemodilution (Fig. 3(d)).

3.4. Tissue oxygen partial pressure [$PtO_2(R)$ and $PtO_2(M)$]

The PtO_2(R) decreased to 8–10 mmHg (51–59% of the b.v.) after the 65% hemodilution, and further declined to 3–5 mmHg (17–28% of the b.v.) after the 30% bleeding (Fig. 4(a)). The administration of HSA showed no improvement, however, the injection of PEG(rHSA–FeP) or RBC immediately increased the PtO_2(R) to 8–9 mmHg (84–97% of the values before the bleeding). In the RBC group, the PtO_2(R) became somewhat higher and reached

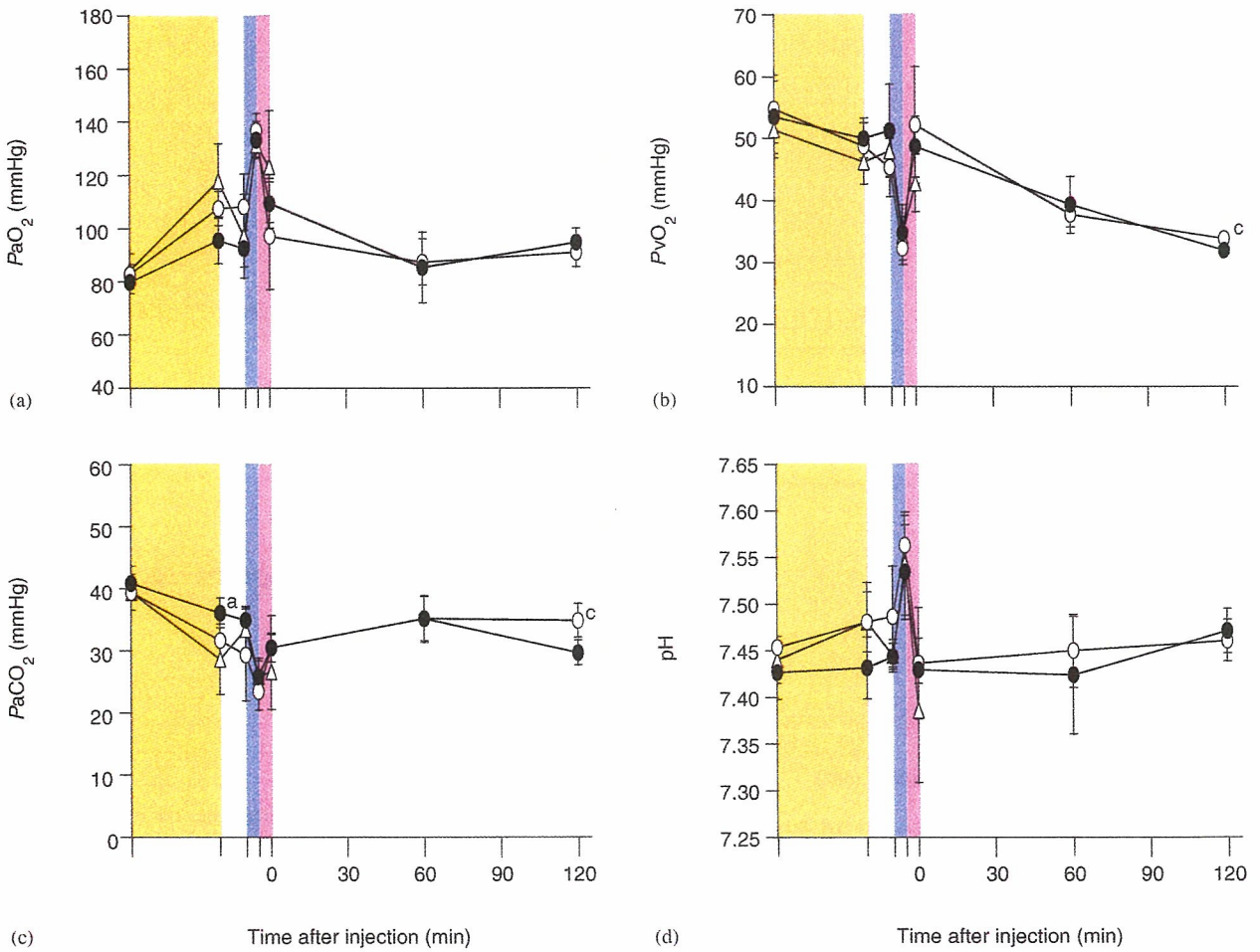

Fig. 3. Effect of PEG(HSA–FeP) solutions on (a) PaO_2, (b) PvO_2, (c) $PaCO_2$, and (d) pH in anesthetized rats subjected to hemodilution and hemorrhage. Each value represents the mean ± SD of 5 rats [●; PEG(HSA–FeP) group, ○; whole blood group, and △; HSA group]. The yellow, blue, and pink areas indicate the periods of 65% hemodilution, 30% bleeding, and sample infusion, respectively. $^{a}p<0.05$ versus HSA group (Tukey–Kramer test) and $^{c}p<0.05$ versus PEG(HAS–FeP) group (Unpaired t-test).

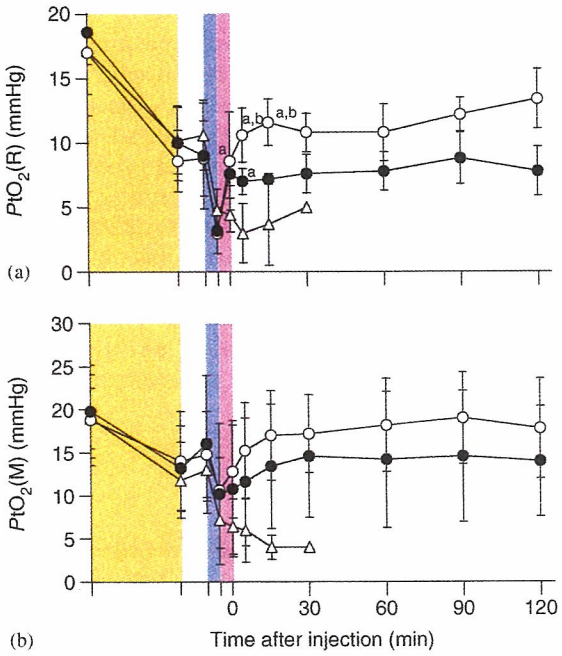

Fig. 4. Effect of PEG(HSA–FeP) solutions on (a) PtO_2(R) and (b) PtO_2(M) in anesthetized rats subjected to hemodilution and hemorrhage. Each value represents the mean ± SD of 5 rats [●; PEG(HSA-FeP) group, ○; whole blood group, and △; HSA group]. The yellow, blue, and pink areas indicate the periods of 65% hemodilution, 30% bleeding, and sample infusion, respectively. $^{a}p<0.05$ versus HSA group (Tukey–Kramer test) and $^{b}p<0.05$ versus PEG(HSA–FeP) group (Tukey–Kramer test).

11 mmHg after 15 min. They both remained constant by the end of the measurements.

The PtO_2(M) decreased to 7–11 mmHg (38–56% of the b.v.) by the 30% bleeding (Fig. 4(b)). The administration of the RBC gradually increased the PtO_2(M) to 17 mmHg (90% of the b.v.) for 15 min, and maintained this level. The transfusion of PEG(HSA–FeP) also slowly increased the PtO_2(M) to 15 mmHg (74% of the b.v.) for 30 min, and the value was stable throughout the experiment.

4. Discussion

4.1. Acute anemia

The isvolemic 65% hemodilution with HSA reduced the Hb concentration, leading to a decrease in the oxygen supply to the tissue. Hypoxia in vital organs and muscle tissues were clearly shown by the declines of MAP, PtO_2(R), and PtO_2(M). The initial response to compensate for this acute anemia is generally an increase in the rate or depth of respiration (hyperventilation); both result in an elevation of the PaO_2 level. In fact, the PaO_2 was increased to 120–140% of the b.v. just after the 65% hemodilution. Since the respiration rate was not changed, we theorized that the increase of depth of respiration is the major factor for the high PaO_2.

4.2. Hemorrhagic shock

During the hemorrhagic shock by the 30% bleeding, significant decreases in the MAP, PvO_2, PtO_2(R), and PtO_2(M) were observed by the loss of the circulation blood volume. The HR and respiration rate also decreased. On the contrary, PaO_2 was increased to about 160% of the b.v., because the RBC has to increase its oxygen saturation. The $PaCO_2$ decreased to about 62% of the b.v. and the pH increased to 7.55. A respiratory alkalosis probably overcomes the metabolic acidosis. The lactate also increased (data not shown), which could be due to the anaerobic metabolism in the peripheral circulation systems.

4.3. Responses to infusion of PEG(HSA–FeP)

The injection of the sample solutions increased the blood volume and improved the circulatory flows. The lactate was washed out from the tissues and into the circulatory system, which decreased the pH to the initial level of 7.43 in all groups. The administration of HSA did not restore any parameters, leading to death within 41 min. In contrast, the infusion of PEG(HSA–FeP) or RBC kept all the rats alive until the end of the measurement.

The circulation half lifetime of FeP (τ_{50}) after the administration of PEG(HSA–FeP) (20% top loading) in anesthetized rats has been determined to be 14 h [8]. The surface modification by PEG significantly prevented the rapid clearance of the incorporated FeP and contributed to increasing the oxygen-transporting efficacy. In this experimental setup, over 80% of the material remained in the bloodstream 120 min after the injection. It is almost the same level as those observed in the 20% top-loading test.

After the injection of PEG(HSA–FeP), the animals showed significant and quick recoveries in MAP, HR, respiration rate, PaO_2, PvO_2, $PaCO_2$, and pH, the same as seen in the RBC group. These results definitely show the oxygen-transporting capability of the PEG(HSA–FeP) solution as a resuscitative fluid. The PvO_2 is a crucial parameter to evaluate the oxygen saturation in blood. The complete restoring of PvO_2 to the level before the bleeding implies a sufficient oxygen supply by PEG(HSA–FeP). The hyperventilation by hypoxia was also depressed and PaO_2 returned to the b.v.

Among the vital organs, renal perfusion is first impaired due to redistribution of the systemic blood flow, so that the PtO_2(R) is a sensitive parameter to the subtle change in the blood circulation and oxygen delivery. The increase in PtO_2(R) by the transfusion of PEG(HSA–FeP) or RBC was very quick, because the oxygen is preferentially supplied to the vital organs. On the other hand, the PtO_2(M) was gradually elevated for 30 min with the stabilization of the blood circulation.

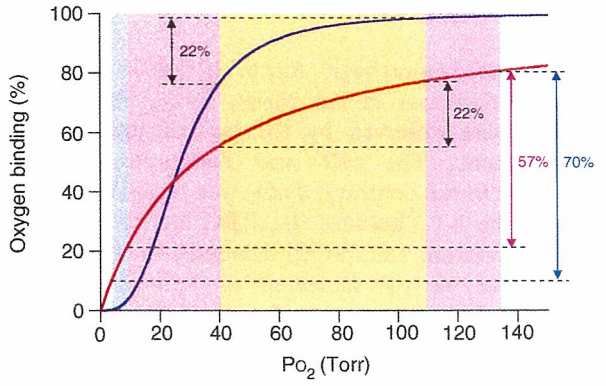

Fig. 5. Oxygen equilibrium curves of PEG(HSA–FeP) (red line) and human RBC (blue line) at 37 °C. The yellow-colored area represents the difference between 110 mmHg at lungs and 40 mmHg at muscle tissues in human. The pink-colored area corresponds to the difference between 134 mmHg of PaO_2 and 9.3 mmHg of PtO_2(M) in hemorrhagic shock state after the 30% bleeding. The left edge of the blue-colored area indicates 3.7 mmHg of PtO_2(R) at the hemorrhagic shock state. The values represented in percent indicate the OTEs.

4.4. Oxygenation of the tissues by PEG(HSA–FeP)

All the physiological responses showed that PEG (HSA–FeP) has the capability to transport oxygen throughout the body. Nevertheless, the restoration effect by PEG(HSA–FeP) in PtO_2(R) and PtO_2(M) was slightly weak compared to that observed in the RBC group. The infusion volume and heme concentration ([heme] = 3 mM) were exactly the same. The oxygen transporting efficiency (OTE) of PEG(HSA–FeP) between the lungs (PO_2 = 110 Torr) and muscle tissues (PO_2 = 40 Torr) (22%) is also identical to the human RBC (Fig. 5) [10]. Therefore, we theorized that the relatively low oxygenation of the renal cortex is due to a Langmuir-type absorption of the oxygen binding of PEG(HSA–FeP); the Hill's coefficient (n) is 1.0. It is well known that human RBC has an allosteric effect on the oxygen-binding equilibrium (n = 3.0) [14]. If the oxygen partial pressure of the peripheral tissue dramatically decreased, a significant difference would appear in the OTEs of PEG(HSA–FeP) and RBC. For instance, in this experimental set up, the 30% blood-bleeding induced extreme low-oxygen partial pressures in the renal cortex (3.7 mmHg) and muscle tissue (9.3 mmHg), and also the high PaO_2 of 134 mmHg. In this situation, the RBC shows maximum OTE of 94–99%, because of the allosteric effect on the oxygen binding to Hb. On the contrary, PEG(HSA–FeP) demonstrated a 57–70% OTE (Fig. 5). This would provide an insufficient oxygen supply to the renal cortex and muscle tissues to some degree, even though the increased PtO_2(R) and PtO_2(M) after the infusion of PEG(HSA–FeP) remained constant for 120 min during the experiment period.

5. Conclusions

The administration of the PEGylated albumin-heme solution into the acute anemia rat model showed a significant efficacy on (i) resuscitation of hemorrhagic shock, (ii) improving the blood circulation, and (iii) oxygen delivery throughout the body. The overall restoration ability of PEG(HSA–FeP) occurred to almost the same extent as that of the RBC suspension. All the systemic responses imply that the PEG(HSA–FeP) solution can be used as an valuable oxygen-carrying plasma expander. The relatively low improvement in PtO_2(R) and PtO_2(M) may be due to the absence of the allosteric effect of the oxygen binding to FeP (n = 1.0). It is also of great interest to design a cooperative oxygen-binding system using a synthetic molecule. This may be an essential issue for constructing the next generation albumin-based artificial RBC substitutes.

Acknowledgements

This work was supported by Health Science Research Grants (Regulatory Science) of the MHLW Japan, Grant-in-Aid for Scientific Research (No. 16350093) from JSPS, and Grant-in-Aid for Exploratory Research (No. 16655049) from MEXT Japan.

References

[1] Riess JG. Oxygen carriers ("blood substitute")—raison d'etre, chemistry, and some physiology. Chem Rev 2001;101:2797–919.
[2] Squires JE. Artificial blood. Science 2002;295:1002–5.
[3] Winslow R. Blood substitutes. London: Elsevier; 2005.
[4] Gould SA, Moore EE, Moore FA, Haenel JB, Burch JM, Sehgal H, et al. The clinical utility of human polymerized hemoglobins as a blood substitute following acute trauma and urgent surgery. In: Tsuchida E, editor. Blood substitutes. Present and future perspectives. Amsterdam: Elsevier; 1998. p. 41–54.
[5] Vandergriff KD, Malavalli A, Wooldrige J, Lohman J, Winslow RM. MP4, a new nonvasoactive PEG-Hb conjugate. Transfusion 2003;43:509–16.
[6] Sakai H, Hara H, Yuasa M, Tsai AG, Takeoka S, Tsuchida E, et al. Molecular dimensions of Hb-based O_2 carriers determine constriction of resistance arteries and hypertension. Am J Phisiol Heart Circ Physiol 2000;279:H908–15.
[7] Sakai H, Horinouchi H, Masada Y, Takeoka S, Ikeda E, Takaori M, et al. Metabolism of hemoglobin-vesicles (artificial oxygen carriers) and their influence on organic functions in a rat model. Biomaterials 2003;25:4317–25.
[8] Huang Y, Komatsu T, Wang RM, Nakagawa A, Tsuchida E. Poly(ethylene glycol)-conjugated human serum albumin including iron porphyrins: surface modification improves the O_2-transporting ability. Bioconjugate Chem 2006;17:393–8.
[9] Sumi A, Ohtani W, Kobayashi K, Ohmura T, Yokoyama K, Nishida M, et al. Purification and physicochemical properties of recombinant human serum albumin. In: Rivat C, Stoltz J-F, editors. Biotechnology of blood proteins, vol. 227. Montrouge: John Libbey Eurotext; 1993. p. 293–8.
[10] Komatsu T, Matsukawa Y, Tsuchida E. Effect of heme structure on O_2-binding properties of human serum albumin–heme hybrids: intramolecular histidine coordination provides a stable O_2-adduct complex. Bioconjugate Chem 2002;13:397–402.
[11] Komatsu T, Yamamoto H, Huang Y, Horinouchi H, Kobayashi K, Tsuchida E. Exchange transfusion with synthetic oxygen-carrying plasma protein "albumin-heme" into an acute anemia rat model

after seventy-percent hemodilution. J Biomed Mater Res 2003;71A: 644–51.

[12] Tsai AG, Vandegriff KD, Intaglietta M, Winslow RM. Targeted O_2 delivery by low-P_{50} hemoglobin: a new basis for O_2 therapeutics. Am J Physiol Heart Circ Physiol 2003;285:H1411–9.

[13] Cabrales P, Tsai AG, Intaglietta M. Microvascular pressure and functional capillary density in extreme hemodilution with low and high plasma viscosity expander. Am J Physiol Heart Circ Physiol 2004;287:H363–73.

[14] Antonini E, Brunori M. Hemoglobin and myoglobin in their reactions with ligands. In: Neuberger A, Tatum EL, editors. North-Holland research monographs. Frontiers of biology, vol. 21. Amsterdam: North-Holland Publisher Co.; 1971. p. 153–87.

Poly(ethylene glycol)-conjugated Phospholipids in Aqueous Micellar Solutions: Hydration, Static Structure, and Interparticle Interactions

Takaaki Sato,[†] Hiromi Sakai,[†] Keitaro Sou,[†] Richard Buchner,[‡] and Eishun Tsuchida[†,*]

Advanced Research Institute for Science and Engineering, Waseda University, Okubo 3-4-1, Shinjuku-ku, Tokyo 169-8555, Japan, and Institut für Physikalische und Theoretische Chemie, Universität Regensburg, D-93040 Regensburg, Germany

Received: October 25, 2006; In Final Form: November 30, 2006

By means of dielectric relaxation spectroscopy (DRS) and small-angle X-ray scattering (SAXS), we have investigated hydration behavior, solvent dynamics, and static structures of aqueous solutions of poly(ethylene glycol)-conjugated distearoyl phosphatidylethanolamine (DSPE-PEG) (molecular weight of PEG: M_{PEG} = 2000, 5000, and 12 000 Da). A quantitative analysis of the bulk-water relaxation amplitude revealed the effective hydration number of a DSPE-PEG molecule per ethylene oxide monomer unit to be ~5.0−5.5, virtually independent of M_{PEG}. The overall hydration number of a DSPE-PEG molecule is ca. 20% higher than that of the corresponding normal PEG (without DSPE). This is attributed to both hydration of a charged head group of phosphoric acid in DSPE and a packing effect of PEG chains into micellar structures. The pair-distance distribution functions, $p(r)$, extracted from the GIFT analysis of SAXS intensities show that the DSPE-PEGs form spherical-like micelles in water having the maximum diameter of ~16, 22, and 31 nm, respectively, for M_{PEG} = 2000, 5000, and 12 000 Da and nearly identical aggregation numbers of 72 (±10%). The DSPE-PEG micelles behave as charged colloids whose interparticle interaction potential can be approximated by the screened Coulomb potential model. The extracted pair correlation function $g(r)$ demonstrates that both electrostatic repulsion induced by the charged head group and excluded volume effects of the fully hydrated PEG layer contribute to repulsive interactions among the PEG-lipid micelles. This should be a key factor for the function of PEG lipids as a stabilizer of liposomes.

1. Introduction

The hydrophobic driving forces, the solvent−water mediated segregating tendency of hydrophobic molecules or units, play a vital role in various self-assembly phenomena, ranging from the formation of molecular clusters to micelles and vesicular structures.[1] One example is the phospholipid vesicle or liposome that has extensively been studied as a drug delivery system since the formation of a vesicular structure was discovered in the suspension of egg-yolk phosphatidylcholine.[2] Some liposomes are now approved for clinical use as antifungal or anticancer therapies.[3] Poly(ethylene glycol) (PEG)-conjugated phospholipids (PEG-phospholipids) have widely been recognized as efficient stabilizers of phospholipid vesicles or liposomes.[4−6]

They are also effective for the vesicles used to encapsulate concentrated hemoglobin (Hb-vesicles, HbV) that have been developed as an artificial oxygen carrier.[7] Sakai, Sou, Tsuchida, and co-workers have confirmed that the surface modification of liposomes by an incorporation of PEG-phospholipids on the surface of HbV is effective for the stabilization of the vesicles. Long-term preservation of HbV dispersions is improved by suppressing the tendency for conventional liposomes to aggregate with subsequent sedimentation.[8,9] The stabilization has also been found to be useful for biocompatibility, microcirculatory blood flow, and prolonged circulation in the blood stream.[10−12] So far, the underlying mechanism of such stabilization has mainly been explained in terms of the steric hindrance or the excluded volume effect of the extended and hydrated PEG chains on the surface,[13] and the fundamental structural and physicochemical properties of PEG-phospholipids in micellar systems were studied by several authors.[14,15] However, specific knowledge of the hydration of PEG chains in PEG-phospholipid micelles and of the geometric profiles of the micelles, that would be of cardinal importance to elucidate the stabilizing mechanism provided by PEG-phospholipids, is still rare.

Here, we investigated static structures and molecular to cooperative dynamics of aqueous solutions of a series of PEG-conjugated phospholipids, aiming at elucidating key properties that contribute to the stabilization of liposomes. The unique combination of dielectric relaxation spectroscopy (DRS) and small-angle X-ray scattering (SAXS) provides an eminent tool to investigate diverse aspects of aqueous PEG-phospholipid solutions, such as hydration behavior, solvent dynamics, static structures, and intermicellar interaction potentials.

Owing to its eminent sensitivity to all kinds of polarization fluctuations occurring in the nano- to picosecond time scales, DRS[16−26] has proven to be a powerful method for scrutinizing the wide-ranged multifaceted dynamical properties of liquids, involving collective dynamics of solvent,[17−19] hydration,[20−22] micellar specific processes,[23,24] and so on. By an elaborate least-squares fitting procedure of the complex dielectric spectrum, the relaxation times and amplitudes for polarization fluctuations of different physical origins can separately be extracted for further quantitative analysis. DRS is generally regarded as a "mature" technique, but it has only recently reached sufficient accuracy and resolution that enables successful application to

* To whom correspondence should be addressed. E-mail: eishun@waseda.jp. Phone: +81-3-5286-3120. Fax: +81-3-3205-4740.
† Advanced Research Institute for Science and Engineering.
‡ Institut fur Physikalische und Theoretische Chemie.

10.1021/jp067011k CCC: $37.00
Published on Web 01/18/2007

ionic and non-ionic micellar solutions typically showing multistep relaxation behavior.[20−24]

On the one hand, SAXS[21,27−37] is a widely applied technique to investigate the structure and interaction potential of colloids, e.g., micelles, vesicles, and proteins, whose length scale is typically within the range of 1∼100 nm. The generalized indirect Fourier transformation (GIFT) technique[32−36] developed by Glatter and co-workers in the past decade as an extension of the well-established indirect Fourier transformation (IFT) technique[29] has renovated situations in small-angle scattering (SAS) data analysis. GIFT allows us to access virtually model-free real space structural information on the nanoassemble systems even for the strongly interacting dense systems.

2. Experimental Section

2.1. Materials. Poly(ethylene glycol)-conjugated phospholipids, 1,2-distearoyl-*sn*-glycero-3-phosphatidylethanolamine-*N*-[monomethoxy-poly(ethylene glycol)], hereafter abbreviated as DSPE-PEG, having PEG of molar mass of 2000, 5000, and 12 000 Da and poly(ethylene glycol)s (PEGs) with molecular masses of 2000, 5000, and 12 000 Da were purchased from NOF Co. (Tokyo, Japan).

2.2. Sample Preparation. Solutions were prepared by weight from solid samples of DSPE-PEG and PEG (M_{PEG} = 2000, 5000, and 12 000 Da) by adding Millipore (Milli-Q) water. According to the procedure of Johnsson et al., DSPE-PEG solutions were incubated at ∼60 °C for about 3 h. These freshly prepared solutions were kept for a half day at ambient temperature for equilibration and were immediately used for dielectric relaxation spectroscopy (DRS) and small-angle X-ray scattering (SAXS) experiments.

2.3. Dielectric Relaxation Spectroscopy (DRS). To obtain specific information about hydration of hydrophilic groups and states of water in aqueous DSPE-PEG systems from the view point of molecular dynamics, we have determined the complex dielectric spectra, $\epsilon^*(\nu) = \epsilon'(\nu) - i\epsilon''(\nu)$, of these aqueous solutions at 25 °C in the frequency range $0.03 \le \nu/\mathrm{GHz} \le 20$ by the use of time domain reflectometry (TDR)[18,19] based on the Hewlett-Packard instruments HP54121A and HP54120B. All time-domain measurements and conversion of the time-domain reflected plus waveforms to the frequency-domain spectrum were made according to the previously reported procedure of Sato and Buchner.[18] For selected systems, the frequency range was expended to the millimeter-wave region by the use of A-band and E-band waveguide interferometry,[26] covering $27 \le \nu/\mathrm{GHz} \le 89$. For the quantitative description of the experimental $\epsilon^*(\nu)$ spectra, we have tested various conceivable relaxation models based on a superposition of n Havriliak−Negami (HN) equations, or its variants, using a nonlinear least-squares fitting procedure

$$\epsilon^*(\nu) = \epsilon_\infty + \sum_{j=1}^{n} \frac{\Delta\epsilon_j}{[1 + (i2\pi\nu\tau_j)^{\beta_j}]^{\alpha_j}} \quad (1)$$

In these models, the jth dispersion step (j = 1, 2, ..., n) is defined by its relaxation time, τ_j ($\tau_j > \tau_{j+1}$), and amplitude, $\Delta\epsilon_j$, where n is the number of the separable dispersion steps. ϵ_∞ is the infinite frequency permittivity, and α_j and β_j are the shape parameters representing asymmetric and symmetric shapes of a spectrum, respectively.

2.4. Small-Angle X-ray Scattering (SAXS). All SAXS experiments were performed using a SAXSess camera (Anton-Paar, Graz, Austria). A PW3830 X-ray generator with a long fine focus sealed glass X-ray tube (PANalytical) was operated at 40 kV and 50 mA. A focusing multilayer optics and a block collimator provide an intense monochromatic primary beam (Cu Kα radiation, λ = 0.154 nm) with negligible background. A semi-transparent beam stop enables measurement of the attenuated primary beam at q = 0. The samples were filled into vacuum-tight thin quartz capillaries and set in a TCS 120 temperature-controlled sample holder unit (Anton Paar). The 2D scattered intensity distribution recorded by an imaging-plate (IP) detector was read out by a Cyclone storage phosphor system (Perkin-Elmer, USA). The 2D data were integrated into the 1D scattering function $I(q)$ as a function of the magnitude of the scattering vector

$$q = \frac{4\pi}{\lambda}\sin(\theta/2) \quad (2)$$

where θ is the total scattering angle.

All $I(q)$ data were normalized so as to have the uniform primary intensity at q = 0 for transmission calibration. The background scattering contributions from capillary and solvent were corrected. The absolute intensity calibration was made by using water intensity as a secondary standard.

2.5. Theoretical Basis of SAXS Data Analysis. The total scattered intensity, $I(q)$, from one-component globular particle systems can generally be formulated as

$$I(q) = n\,P(q)\,S(q) \quad (3)$$

where n is the particle density, $P(q)$ is the averaged form factor, and $S(q)$ is the static structure factor. SAXS observes the structure of nanoparticles via the convolution square (or the spatial autocorrelation function) of the electron density fluctuations

$$\gamma(r) \equiv \Delta\tilde{\rho}^2(r) = \langle\Delta\tilde{\rho}^2(\boldsymbol{r})\rangle = \left\langle\int_{-\infty}^{\infty}\Delta\rho(\boldsymbol{r}_1)\Delta\rho(\boldsymbol{r}_1 - \boldsymbol{r})\,d\boldsymbol{r}_1\right\rangle \quad (4)$$

where $\Delta\rho(\boldsymbol{r})$ is the electron density fluctuation at the position $\boldsymbol{r}$, and r is the distance between two scattering centers chosen inside the particle. The so-called pair-distance distribution function (PDDF), defined as $p(r) = \gamma(r)\,r^2$, is an essential real-space function that contains information on the geometry (size and shape) as well as the internal density fluctuation of the particle. $P(q)$ is the reciprocal-space coordinate associated with $p(r)$, and they are connected via the Fourier transformation

$$P(q) = 4\pi\int_0^\infty p(r)\frac{\sin qr}{qr}\,dr \quad (5)$$

The static structure factor $S(q)$ embodies a (time-averaged) length-scale dependent (particle) density fluctuation and therefore offers information about interparticle potentials of colloidal systems. $S(q)$ is given by the Fourier transformation of the total correlation function, $h(r) = g(r) - 1$, as

$$S(q) = 1 + 4\pi n\int_0^\infty [g(r) - 1]r^2\frac{\sin qr}{qr}dr \quad (6)$$

where $g(r)$ is the pair-correlation function. The SAXS data for aqueous DSPE-PEG solutions were analyzed by the generalized indirect Fourier transformation (GIFT) technique.

3. Results and Discussions

3.1. Dielectric Relaxation Behavior of Aqueous DSPE-PEG Solutions. In Figure 1, we present representative complex

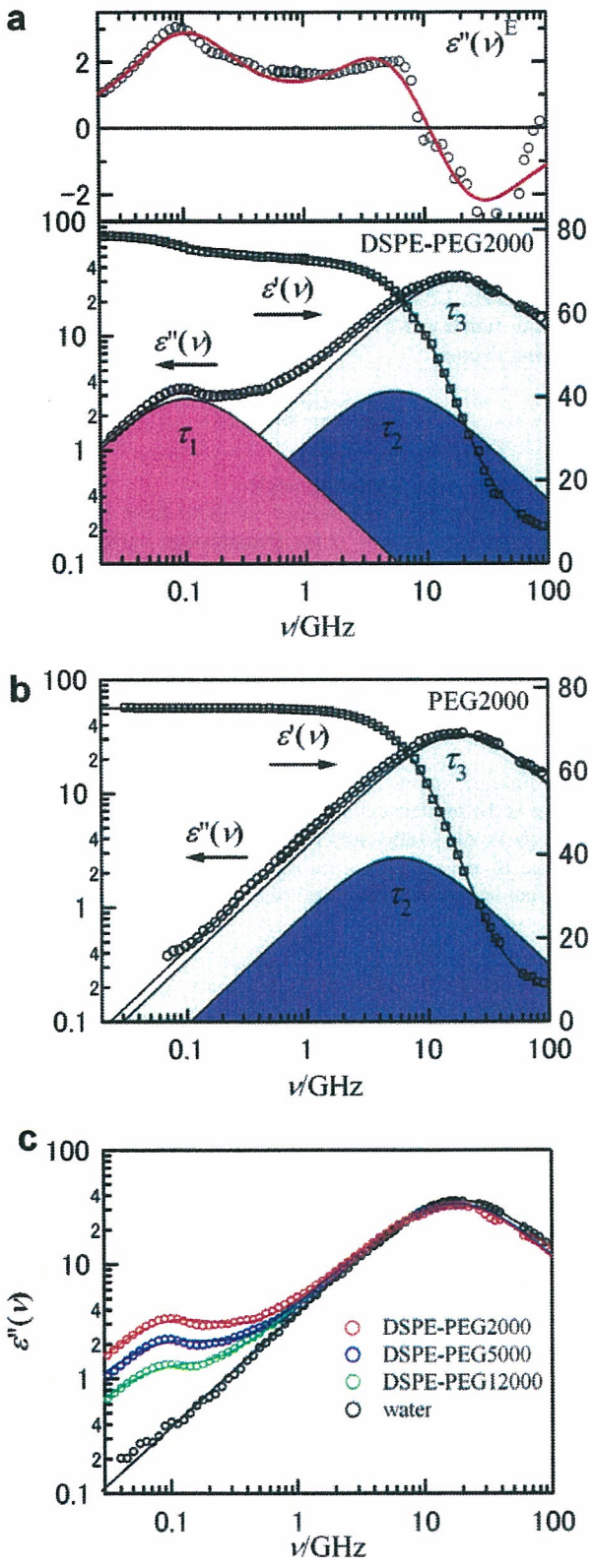

Figure 1. The complex dielectric spectra of aqueous DSPE-PEG and PEG solutions in $0.03 \leq \nu/\mathrm{GHz} \leq 89$ at 25 ± 0.03 °C. The spectrum of aqueous DSPE-PEG at polymer concentration $c = 7.1$ g dL^{-1} (a) and that of PEG at $c = 5.1$ g dL^{-1} (b), corresponding to $W_{\mathrm{PEG}} = 0.05$. In the upper panel of (a), the excess loss spectrum defined as $\epsilon''(\nu)^{\mathrm{E}} = \epsilon''(\nu) - \epsilon_{\mathrm{w}}''(\nu)$ is also shown, where $\epsilon_{\mathrm{w}}''(\nu)$ is an ideal bulk-water loss spectrum scaled according to analytical water concentration $c_{\mathrm{w}}(c)$. The comparison among DSPE-PEGs with different molecular masses of PEG, $M_{\mathrm{PEG}} = 2000$, 5000, and 12 000, at fixed $W_{\mathrm{PEG}} = 0.05$ (c), where the water spectrum from ref 17 is also shown for comparison.

dielectric spectra of aqueous DSPE-PEG and PEG solutions at 25 °C. An addition of either DSPE-PEG or PEG to water induces a pronounced broadening of the $\epsilon^*(\nu)$ spectrum on the lower frequency side of the loss peak frequency; the loss peak frequency centered at ~19 GHz remains virtually unchanged. The interferometry data covering up to 89 GHz confirm that there is no significant broadening of the high-frequency part of the spectrum. Thus, the low-frequency broadening is not likely due to a Cole−Cole-like relaxation-time distribution of the bulk water process but is validly attributed to the emergence of a new slow process. This also confirms the validity of the interpretation given in a recent dielectric study of Shikata et al.[22] on aqueous poly(ethylene oxide)s, where the frequency coverage was limited up to 20 GHz.

The observation of an almost constant loss peak frequency is fairly different from that of the situation for, e.g., alcohol/water mixtures,[18,19] where the loss peak frequency is continuously and rapidly sifted to lower frequencies with increasing solute concentration. The excess loss spectrum shown in the upper panel of Figure 1a indicates that, without imposing any relaxation model, two additional relaxation processes emerge upon addition of DSPE-PEG that are centered at ~100 MHz and ~5 GHz. Simultaneously, a negative excess polarization fluctuation appears for bulk-water relaxation without exhibiting a significant shift of the loss peak frequency. As for the results of the fitting procedure, we confirmed that a superposition of three Debye ($j = 3$) relaxation processes described as

$$\epsilon^*(\nu) = \epsilon_\infty + \sum_{j=1}^{3} \frac{\Delta\epsilon_j}{1 + 2i\pi\nu\tau_j} \tag{7}$$

gives the best description to the spectra for all the aqueous DSPE-PEGs (MPEG = 2000, 5000, and 12 000) and a consistent set of fitting parameters, whereas the corresponding normal PEG (without DSPE) solutions show only two dispersion steps, lacking the well-pronounced 100 MHz dispersion for DSPE-PEG solutions.

Figures 2 and 3 show the relaxation times τ_j and amplitudes $\Delta\epsilon_j$ of aqueous DSPE-PEG and PEG solutions, respectively. The relaxation times of the dominating high-frequency process, τ_3, of both DSPE-PEG and PEG solutions, are practically identical to that of the main dispersion of pure water, $\tau_{\mathrm{D}} = 8.3$ ps, and almost independent of polymer concentration, c, and molecular weight, M. As demonstrated by Figure 3, the amplitude, $\Delta\epsilon_3$, smoothly decreases from that for pure water with increasing c. Thus, the assignment of the τ_3-process is straightforward; this can clearly be attributed to the cooperative rearrangement of the hydrogen-bond network of bulk-like water. Note that, as already indicated by the negative excess loss spectrum at high-frequencies and demonstrated by Figure 3a, $\Delta\epsilon_3$ always exhibits smaller values than expected from analytical water concentration.

Neither the intermediate relaxation nor the lowest-frequency one can be attributed to the rotational diffusion of a whole DSPE-PEG micelle because τ_1 and τ_2 are too small if referring to the prediction of the Stokes−Einstein−Debye (SED) equation for the micellar radius determined from SAXS experiments (cf. Section 3.3). The τ_2-process centered at 5−6 GHz cannot necessarily be attributed to a micelle-specific process because the features are common to DSPE-PEG and normal PEG solutions. Judging from the time scale of τ_2, which is greater than that of bulk-water relaxation by a factor of 3 to 4, and from the behavior of $\Delta\epsilon_2$, which almost proportionally increases with c, the intermediate τ_2-relaxation is related to cooperative

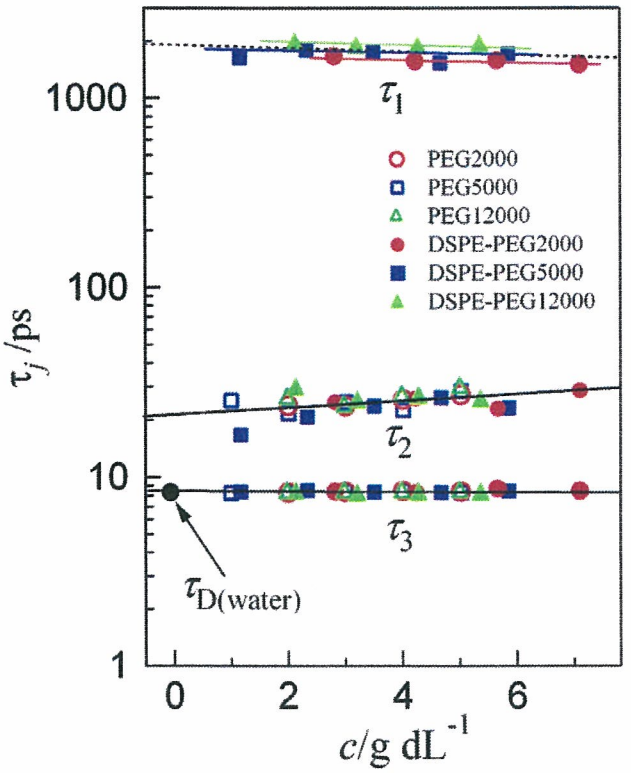

Figure 2. Dielectric relaxation times of aqueous solutions of DSPE-PEG and PEG for $M_{PEG} = 2000$, 5000, and 12 000 at 25 °C as a function of polymer concentration, c.

molecular motions in hydrated PEG layers. This is in line with the interpretation of dielectric spectra of the water/poly(oxyethylene) alkylether system given by Schrödle et al.[20] The process must be highly cooperative in the densely packed hydrated PEG layer because the conformational change of the poly(oxyethylene) chains and displacement of water molecules are required to occur simultaneously, leading to the sufficiently slower dielectric relaxation time compared to that of bulk water.

The low-frequency relaxation process characterized by $\tau_1 \sim 2$ ns (loss peak frequency ~ 0.1 GHz) exists only for DSPE-PEG systems, as clearly illustrated in Figure 1. The finding indicates that the possible assignment is either to micellar- or DSPE-specific processes. As shown in Figure 3b, if we re-plot $\Delta\epsilon_1$ as a function of the molar concentration of the DSPE-PEGs, the data for different M_{PEG} perfectly collapse on the same straight line. Thus, this relaxation has to be assigned to the rotation of the charged DSPE head group. This interpretation is well supported by the data of Katzee et al.[24] A slightly larger τ_1 for higher M_{PEG} may reflect the stronger frictional forces for head group rotation with longer PEG chains.

3.2. Hydration of DSPE-PEG Micelles. Using the experimentally obtained bulk-water amplitude, $\Delta\epsilon_3$, we estimated the effective hydration number of the DSPE-PEG molecule and that for the corresponding PEG.

The generalized Cavell equation[25]

$$\Delta\epsilon_i = \frac{\epsilon}{3(\epsilon + (1-\epsilon)A_i)} \frac{N_A}{k_B T \epsilon_0} \frac{g_i \mu_{Gi}^2}{(1-\alpha_i f_i)^2} c_i \qquad (8)$$

connects the relaxation amplitude of the ith process, $\Delta\epsilon_i$, to the concentration of the relaxation species, c_i, where μ_{Gi} is a gas-phase dipole moment, α_i a polarizability, f_i the field factor, A_i

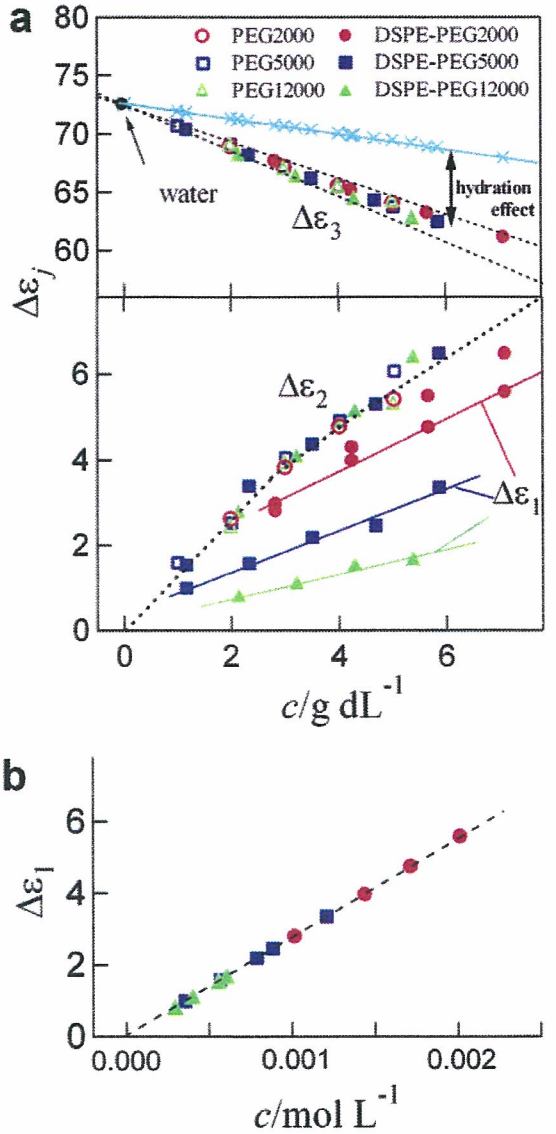

Figure 3. The relaxation amplitudes for aqueous solutions of DSPE-PEG and normal PEG with $M_{PEG} = 2000$, 5000, and 12 000 at 25 °C as a function of polymer concentration in g dL^{-1} (a) and $\Delta\epsilon_1$ replotted as a function of molar concentration of DSPE-PEG (b). A light blue colored solid line shown together with $\Delta\epsilon_3$ in panel a represents the ideal bulk-water amplitude calculated from analytical water concentration under the assumption that all water molecules in solution contribute to the bulk-water process with the same Kirkwood dipole−dipole orientational correlation factor as pure water.

the shape parameter of the reaction field, ϵ the static permittivity, g_i the dipole−dipole correlation factor, k_B the Boltzmann constant, N_A the Avogadro's number, and ϵ_0 the vacuum permittivity.

Equation 8, normalized to pure water, yields the apparent water concentration at polymer concentration c, $c_w^{app}(c)$, as

$$c_w^{app}(c) = c_w(c)\frac{g_w(c)}{g_w(0)} = \frac{\epsilon(0)(2\epsilon(c)+1)}{\epsilon(c)(2\epsilon(0)+1)} \frac{(1-\alpha_w f_w(c))^2}{(1-\alpha_w f_w(0))^2} \frac{\Delta\epsilon_w(c)}{\Delta\epsilon_w(0)} c_w(0) \qquad (9)$$

where $\Delta\epsilon_w(0) = 72.5$ and $\Delta\epsilon_w(c) = \Delta\epsilon_3(c)$. Assuming a spherical water molecule ($A_i = 1/3$) having a radius $r = 0.1425$

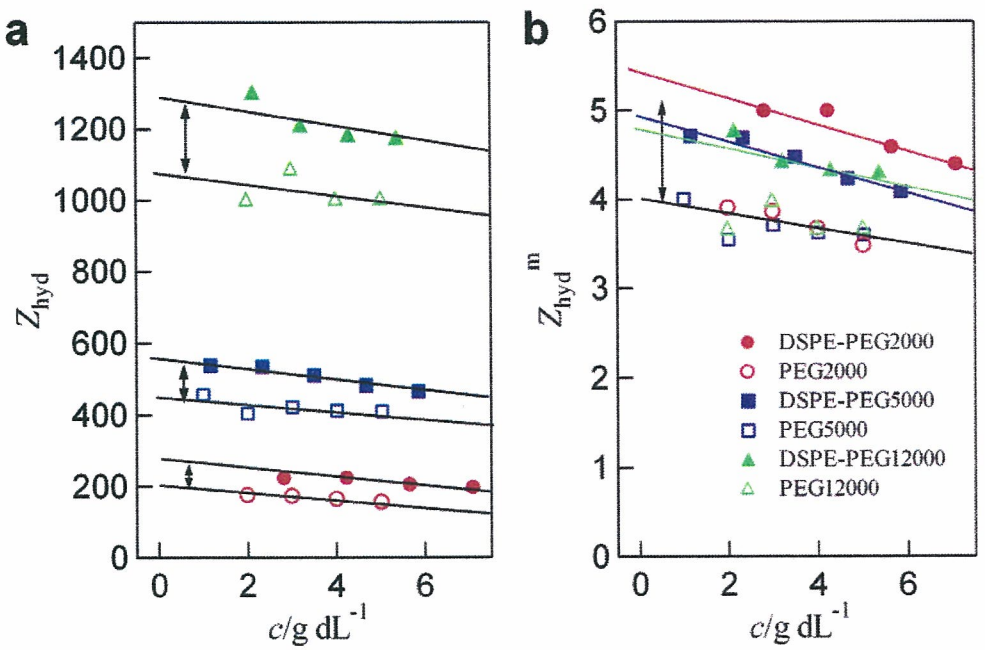

Figure 4. The effective hydration number of DSPE-PEG and PEG molecules, Z_{hyd} (a), and those per ethylene glycol monomer unit, Z_{hyd}^m (b), as a function of polymer concentration, c. These quantities are calculated from the concentration dependence of the dispersion amplitude of the bulk-water process, $\Delta\epsilon_3$. Z_{hyd} explains the number of water molecules that cannot contribute to the bulk-water process due to the hydration effects.

nm and a polarizability $\alpha_w = 1.607 \times 10^{-40}$ Cm^2/V, the apparent concentration of bulk water, $c_w^{app}(c)$, i.e., the concentration of water molecules contributing to the bulk-water relaxation process, can be deduced. We define the effective hydration number of a polymer molecule, Z_{hyd}, or that per PEG monomer unit, Z_{hyd}^m, by converting the difference between the apparent water concentration, $c_w^{app}(c)$ and analytical water concentration, $c_w(c)$, to the corresponding number of water molecules per DPSE-PEG molecule

$$Z_{hyd} = |c_w(0) - c_w^{app}(c)|/c \qquad (10)$$

or that per EG monomer unit, $Z_{hyd}^m = Z_{hyd}/N$, where N is the degree of polymerization of PEG. According to the definition, using the magnitude of polarization fluctuations as a suitable measure, Z_{hyd} gives the number of water molecules that cannot contribute to the bulk-water relaxation process due to the hydration effects, which significantly slow down their intermolecular collective dynamics.

In Figure 4, Z_{hyd} and Z_{hyd}^m are plotted as a function of c. Z_{hyd} for all the investigated solutions seems to be a gradually decreasing function of c, giving the Z_{hyd}^m value of 5.0−5.5 ($c \to 0$) for all DSPE-PEGs and ~4 ($c \to 0$) for the corresponding PEGs as shown in Figure 4b. This demonstrates that approximately 5.0−5.5 hydrated water molecules per EG unit are as tightly bound as they show significant slowing down and consequently lose the nature of bulk water. The systematically higher Z_{hyd} values for DSPE-PEG than those for the corresponding normal PEG indicate that the difference is not likely to be related simply to the additional hydration water to the DSPE charged head group. If the difference of Z_{hyd} values was solely attributed to the hydration of the phosphatidylethanolamine group, the effect should become less pronounced with increasing M_{PEG} due to relatively smaller contribution of the DSPE head group hydration compared to dominating long-chain PEG hydration. However, we can see the significant difference, ~200, for $M_{PEG} = 12\,000$, well within the accuracy of our DRS experiments/analysis. Also, a hydration number of ~200 for phosphatidylethanolamine group would be too large to be accommodated around the phosphatidylethanolamine group. Therefore, we conclude that not only excess hydration water molecules to the DSPE charged head group, but packing effects of PEG into a micellar structure also contribute to higher Z_{hyd} values for DSPE-PEG than those for normal PEG.

Direct numerical comparison of Z_{hyd} with literature values is rather restricted because of the lack of appropriate references. However, NMR studies of Nilsson and Lindman on poly(oxyethylene) alkylether (often abbreviated as C_iE_j) in D_2O yielded hydration numbers in the range of 5 to 6 from the translational self-diffusion constant of D_2O.[37] Recently, Schrödle et al.[20] made an extensive dielectric study on aqueous $C_{12}E_5$, for both aqueous micellar and liquid crystalline phases and obtained about 3.5 to 4.0 bound water molecules per ethylene glycol (EG) monomer unit for micellar soultions. Using DRS also, Sato et al. reported that, for aqueous poly(oxyethylene) cholesteryl ether (ChE_j with $j = 10$ and 15), each oxyethylene unit is hydrated by approximately 4 to 4.5 water molecules at ambient condition.[21] The latter evaluation is in better agreement with the present Z_{hyd}^m for the DSPE-PEGs. Apparently, there is some dependence of the oxyethylene group hydration on the chain length j for short-chain PEGs in surfactants. The present results on DSPE-PEG solutions also fit into the existing set of PEG hydration numbers. Besides the contribution of direct phosphatidylethanolamine group hydration, the slightly higher hydration number possibly reflects a different packing of DSPE-PEG molecules into the micelles compared to C_iE_j surfactants. The present Z_{hyd}^m for normal PEGs is comparable with the recent estimation of Shikata et al.[22] by DRS on aqueous poly(ethylene oxide)s.

Anyway, for sufficiently long oxyethylene chains, on average 4−5 water molecules are hydrated per EG monomer unit irrespective of the type of hydrophobic group, and this number

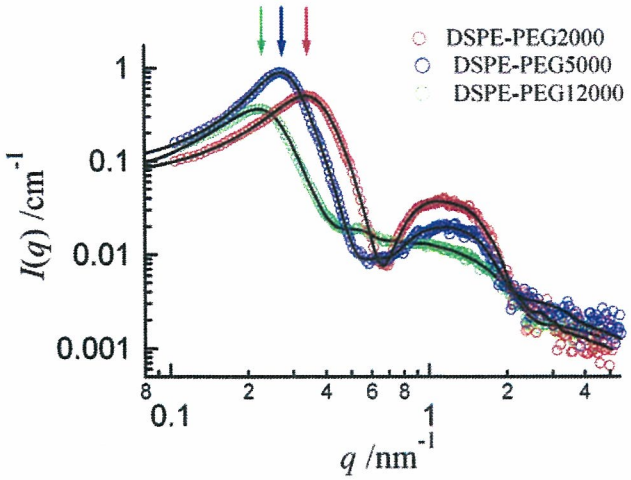

Figure 5. The absolute X-ray scattered intensities $I(q)$ of the aqueous DSPE-PEG solutions with $M_{PEG} = 2000$, 5000, and 12 000 at $W_{DSPE-PEG}$ (weight fraction of DSPE-PEG) = 0.04 at 25 °C. The arrows indicate the intermicellar correlation peak positions q^*, where the distance $d^* = 2\pi/q^*$ gives a measure of center-of-mass to center-of-mass distance of the micelles.

may be almost universal for all PEG-based surfactant systems. Namely, the hydration of the PEG chain is basically governed by the hydration of each EG monomer, and the total hydration number of a polymer or a micelle is approximately given by the simple sum of hydrated water molecules to each EG monomer unit. These hydrated water molecules must contribute to the compressibility of the system and repulsive interaction between the micelles inducing steric hindrance effect.

3.3. The Static Structures of DSPE-PEG Micelles. Figure 5 shows the (collimation-corrected) absolute X-ray scattered intensities $I(q)$ for the aqueous solutions of DSPE-PEG with $M_{PEG} = 2000$, 5000, and 12 000, respectively, at a weight fraction of DSPE-PEG, $W_{DSPE-PEG} = 0.04$. The experimental $I(q)$ of all DSPE-PEG solutions clearly shows the typical features of a scattering function from globular particles. The scattering vector q^*, corresponding to the apparent low-q peak position in $I(q)$, provides a semiquantitative estimation of the averaged intermicellar (i.e., center-of-mass to center-of-mass) distance d^* without imposing any interaction potential model. If we simply extend the idea of Bragg reflections, d^* is approximated as $2\pi/q^*$. As we will show later using a quantitative $S(q)$ analysis, this leads to a small systematic overestimation of d^*. As highlighted by arrows, q^* is shifted to lower-q values with rising M_{PEG}, resulting in $d^* = 19$, 24, and 28 nm, respectively, for $M_{PEG} = 2000$, 5000, and 12 000. To extract more specific information about the micellar structure (size, shape, and internal core−shell structure) as well as the intermicellar interaction potentials, we need further quantitative analysis of the scattering functions. As will be shown below, the GIFT technique[21,30−36] offers an excellent route to access to these quantities.

The SAXS data for aqueous DSPE-PEG solutions were analyzed by the generalized indirect Fourier transformation (GIFT) technique. $P(q)$ and $S(q)$ were simultaneously determined, leaving $P(q)$ model-free, whereas the choice of a plausible interaction potential model and an appropriate closure relation were necessary for $S(q)$. In Figure 6, we display the results of the GIFT analysis.

Within the framework of the mean-spherical approximation (MSA),[38] the direct correlation function $c(r)$ is related to the particle potential $v(r)$ as

$$c(r) = -\beta\, v(r) \qquad (11)$$

where $\beta = 1/k_BT$. $S(q)$ for aqueous DSPE-PEG solutions is calculated assuming a screened Coulomb (Yukawa) potential

$$\beta\, v(r) = \frac{Z_{eff}^2 e_0^2}{4\pi\epsilon\epsilon_0 k_B T}\cdot\frac{-e^{-\kappa(r-\sigma)}}{r(1+\kappa\sigma/2)^2} \quad r > \sigma$$
$$= \infty \quad r < \sigma \qquad (12)$$

where e_0 is the elementary charge, Z_{eff} the effective charge number of the particle, σ the hardsphere diameter, and ϵ the static dielectric constant of the solvent. When there is no salt added, the reciprocal Debye screening length κ is determined by

$$\kappa^2 = \frac{e_0^2}{\epsilon\epsilon_0 k_B T} n Z_{eff} \qquad (13)$$

where n is the number density of the particle, and nZ_{eff} is the net charge of released counter ions in unit volume. We numerically solved the Ornstein−Zernike (OZ) equation[39]

$$h(r) = c(r) + n\int d\mathbf{r}'\, c(|\mathbf{r}-\mathbf{r}'|)\, h(\mathbf{r}') \qquad (14)$$

by employing the Rogers−Young[40] (RY) closure relation

$$g(r) = e^{-\beta v(r)}\left\{1 + \frac{1}{f(r)}[e^{f(r)(h(r)-c(r))} - 1]\right\} \qquad (15)$$

where $f(r) = 1 - \exp(-\alpha r)$ is the mixing function. When $\alpha \to 0$ and $\alpha \to \infty$, RY coincides respectively with Percus−Yevick[41] (PY) and hypernetted chain (HNC). The mixing parameter is adjusted so as to attain the self-consistency of the thermodynamic parameters calculated via the fluctuation root and the virial root.

In Figure 7, the pair-distance distribution functions, $p(r)$, for the DSPE-PEG micelles are shown, where $p(r)$ was obtained as an inverse Fourier transformation of $P(q)$. From the r-value at which $p(r)$ goes to zero, the total diameter of the DSPE-PEG micelle, the so-called D_{max}, is obtained. The low-r local maximum and minimum in $p(r)$ come essentially from the convolution of the negative and positive electron density fluctuations, respectively, of the hydrophobic core and hydrophilic shell of the micelles. It is well-established that, even when these local maximum and minimum do not clearly show up but only appear as a low-r bump due to a relatively good contrast of the core−shell structure, the distance corresponding to the inflection point located on the higher-r side of the local minimum gives a semiquantitative measure of the hydrophobic core diameter, D_C. This holds even when the micelle is highly elongated. Furthermore, the distance between the local maximum and minimum almost universally coincides with $D_C/2$, so that this point can provide a semiquantitative measure of the core radius, r_C. Accordingly, we found that, for all the investigated DPSE-PEG solutions, the deduced D_C and r_C are 5.0 and 2.5 nm, respectively, which is virtually independent of M_{PEG}. Taking molecular volumes from literatures,[42,43] the partial volume of the hydrocarbon group of DSPE, V_{hc}, is calculated as $V_{hc} = 1.016$ nm.[3] If we estimate the aggregation number of DSPE-PEG molecules into micellar structure, according to $N_{agg} = 4\pi r_c^3/3V_{hc}$, we obtain $N_{agg} \sim 72$. This estimation may involve about 10% of error due to spatial resolution of our SAXS measurements and analysis, but the N_{agg} value is very close to the aggregation number of about 75 for DSPE-PEG2000 and DSPE-PEG5000 obtained by static light scattering (SLS) experiments in the pioneer work of Jonsson et al.[14]

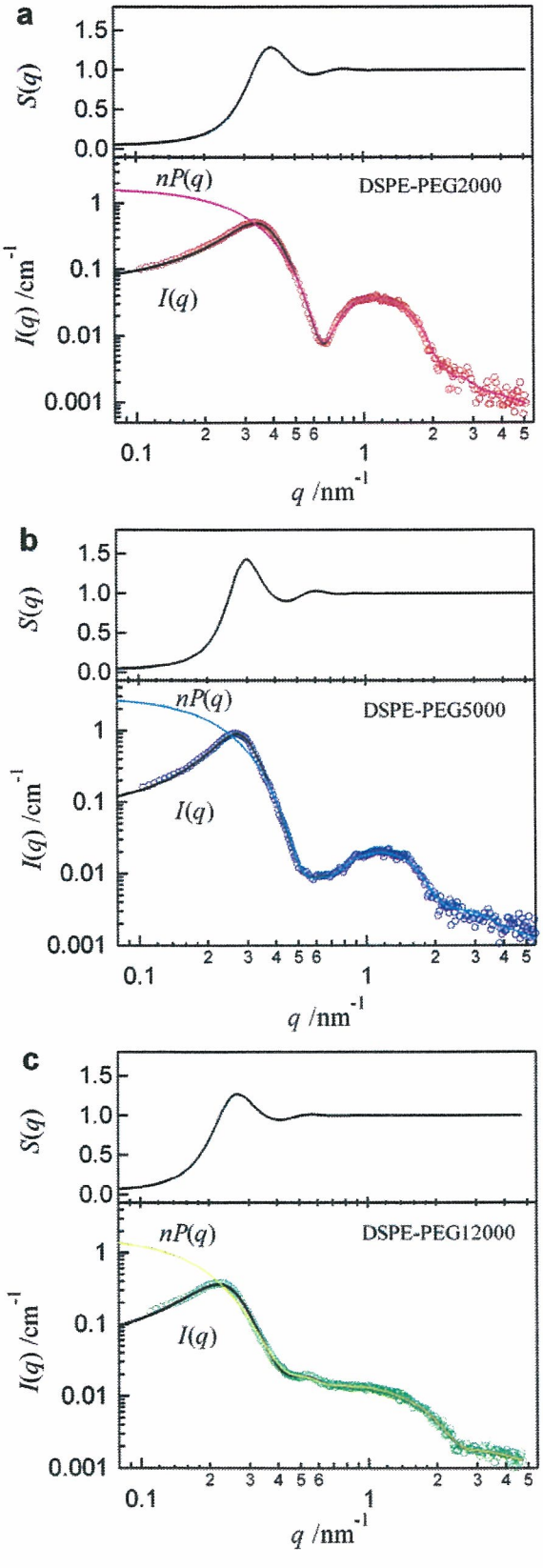

Figure 6. GIFT analysis of the X-ray scattered intensities $I(q)$ of aqueous DSPE-PEG solutions at $W_{DSPE-PEG} = 0.04$ at 25 °C for M_{PEG} = 2000 (a), 5000 (b), and 12 000 (c). Black solid and colored solid curves in the lower panel represent GIFT fit to $I(q)$ and the calculated form factor for n particles existing in unit volume, $nP(q)$, respectively. Also shown in the upper panel is the static structure factor $S(q)$ calculated assuming a screened Coulomb (Yukawa) potential model and Rogers−Young (RY) closure relation.

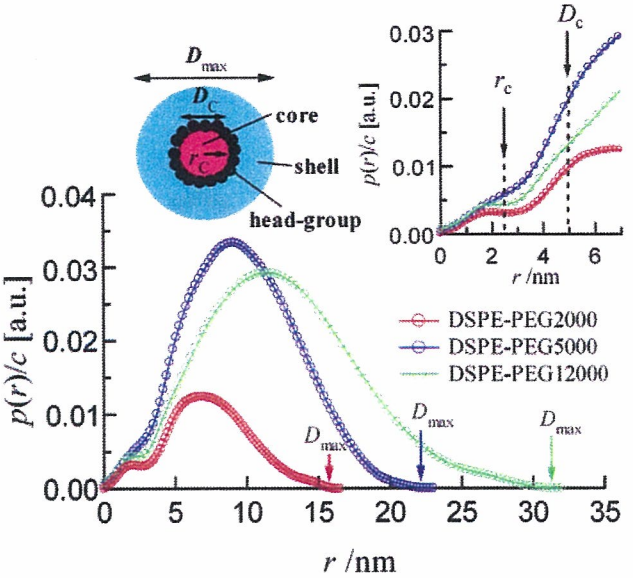

Figure 7. Particle characterization of the DSPE-PEG micelles. The normalized pair-distance distribution functions by polymer molar concentration, $p(r)/c$, for aqueous DSPE-PEG solutions with M_{PEG} = 2000, 5000, and 12 000 at $W_{DSPE-PEG} = 0.04$. The enlarged view in the low-r region is also presented in the inset. The two inflection points in $p(r)$ highlighted by two arrows can be the prominent measure of the core radius, r_c, and diameter, D_c, from which $r_c = 2.5 \pm 0.1$ nm is deduced for all M_{PEG}. This implies nearly identical aggregation numbers for all DSPE-PEG micelles despite the considerable variation of hydrophilic PEG chain length.

Figure 8 presents the number of water molecules existing in different states when involved into a DSPE-PEG micelle and the resulting fraction, ϕ_{bulk}, of the micelle volume occupied by bulk water. The difference between the total number of water molecules exiting in the micelle (per DSPE-PEG molecule), Z_{mic}^{m}, estimated from micellar geometry, and the effective hydration number of a DSPE-PEG molecule, Z_{hyd}^{m}, provides the number of water molecules that still preserve the nature of bulk water, despite penetrating the area of the PEG hydrophilic groups of the micellar structure. Those water molecules are situated in the region $r_C < r < D_{max}/2$ from the center of micelle. ϕ_{bulk} is calculated as $\phi_{bulk} = 1 - [N_{agg}(V_{DSPE-PEG} + V_{hyd})]/V_{mic}$, where $V_{mic} = 4\pi(D_{max}/2)^3/3 = \pi D_{max}^3/6$ is the micellar volume. V_{hyd} is the volume occupied by the water molecules hydrated to a DSPE-PEG molecule, deduced from DRS as shown in Figure 4a, and $V_{DSPE-PEG}$ is the molecular volume of DSPE-PEG. N_{agg} is fixed to 72.

The combined DRS/SAXS analysis clearly reveals that, as shown in the upper panel of Figure 8, a significant amount of water molecules residing inside the head group area of the micelle, indeed reaching 60−75% volume of the total volume of the micelle, still preserves the nature of bulk water. This means that the interpretation of the structure of DSPE-PEG micelles as perfect charged hard spheres (HS) of diameter D_{max} is obviously too simplified. The pronounced increase of ϕ_{bulk} with increasing M_{PEG} demonstrates that more "diluted" or compressible micelles are formed for longer PEG chains, which are essentially stretched. With increasing M_{PEG}, such an open structure will allow easier mutual penetration or overlap of the hydrated PEG layers of approaching micelles.

In Figure 9, we display the pair-correlation functions $g(r)$ for the DSPE-PEG micelles, which are deduced from $S(q)$ analysis of the GIFT procedure. In view of the above results, it is certainly not possible to reproduce SAXS data of the DSPE-PEG solutions using a hard sphere (HS) interaction potential

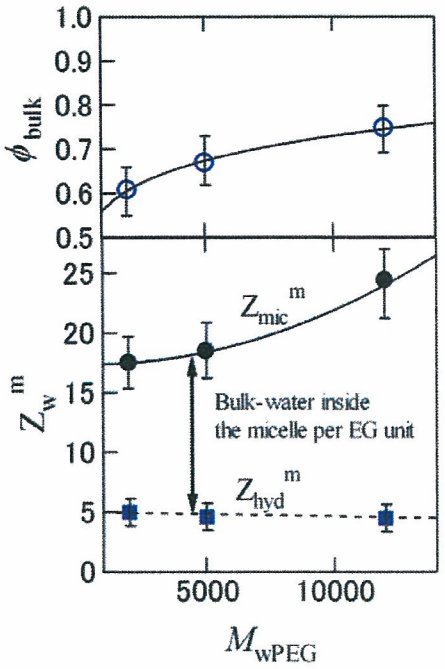

Figure 8. The amount of water molecules in different states involved into a DSPE-PEG micelle for different M_{PEG} as obtained by SAXS and DRS. The lower panel shows the total number of water molecules per EG monomer, Z_{mic}^m, that reside within the micelle (i.e., for $r < D_{max}/2$) according to SAXS, and the effective hydration number per EG unit, Z_{hyd}^m, of a DSPE-PEG molecule deduced from DRS. Because Z_{hyd}^m represents the number of tightly bound, thus slowly relaxing water molecules, the difference between Z_{mic}^m and Z_{hyd}^m gives the number of "bulk-water" molecules (per EG monomer) in the micelle, Z_{bulk}^m. The upper panel displays the resulting fraction, ϕ_{bulk}, of the micelle volume occupied by bulk water.

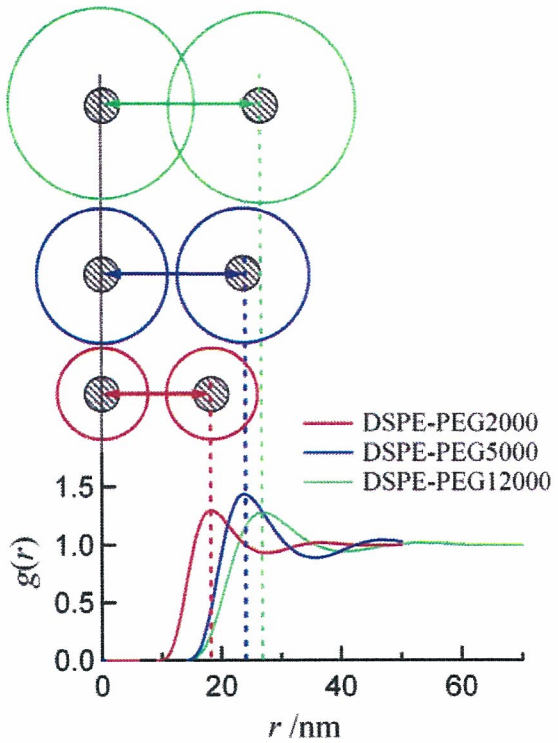

Figure 9. The pair-correlation functions $g(r)$ for the DSPE-PEG micelles (M_{PEG} = 2000, 5000, and 12 000) in water at $W_{DSPE-PEG}$ = 0.04 as obtained by GIFT analysis of SAXS intensities $I(q)$, assuming a screened Coulomb (Yukawa) potential and the Rogers−Young (RY) closure relation. On the same spatial scale, the schematic picture of the micelles is drawn to visualize the interplay between the intermicellar (average) distance and the micellar geometry, where the shaded circle represents a hydrophobic core having $r_c \sim 2.5$ nm.

model for $S(q)$. Although we found that the shape of $S(q)$ can be approximated by a screened Coulomb (Yukawa) potential, one has to recognize that the produced $S(q)$ parameters cannot necessarily be exact. The major reason is that the charges of the DSPE head groups are not on the surface of micelles but are highly localized close to the hydrophilic/hydrophobic interface, whereas the total size of the micelles is far bigger than that of the effective charged sphere, consisting of a hydrophobic core and charged head groups. Furthermore, we cannot exactly define the static dielectric constant of the hydrated PEG layer due to its definition as a macroscopic quantity. However, its anticipated lower (effective) value compared to pure water will give rise to a larger strength but shorter screening length for the electrostatic repulsion between the effective charged spheres than one would obtain when the charged spheres were directly put into water. Of course, the excluded volume effect caused by DPSE-PEG polymers in themselves and hydrated water molecules also greatly contribute to the intermicellar repulsive interaction and osmotic compressibility of the systems. Therefore, it is apparent that a DSPE-PEG micelle cannot be treated as an ideal charged colloid in water. Nevertheless, the extracted g(r), shown in Figure 9, provides an intuitive picture of spatial correlations of these micelles, giving insights into the interplay between the intermicellar distance and the micellar geometry. Note that the pronounced peak positions in $g(r)$ more or less coincide with d^* obtained with a potential model-free approach; see Figure 5. This indicates that the discussion made here is not biased by an approximate modeling of $S(q)$.

At the investigated concentrations, an overlap and interpenetration of hydrated PEG layers eventually occur among DSPE-PEG12000 micelles, whereas a direct contact of micelles hardly takes place for DSPE-PEG2000 and DSPE-PEG5000. Owing to the low ionic strength and the relatively small micellar radii of DSPE-PEG2000 and DSPE-PEG5000, long-range electrostatic repulsion is strong enough to keep the relatively small micelles apart. Figure 9 reveals that at low ionic strength both an electrostatic repulsion induced by the charged head group and an excluded volume effect of the hydrated PEG layer contribute to the net repulsive interaction among the PEG-lipid micelles, which must be an essential factor for the function of PEG-lipids as a stabilizer of liposomes. It is naturally anticipated that, at higher ionic strength, such as a physiological condition, the steric hindrance induced by hydrated PEG chains becomes more and more dominant over the efficiently screened electrostatic repulsion for the interparticle repulsive interaction of PEG-lipid micelles. We consider that the main conclusion of Jonsson et al.[14] (that the electrostatic intermicellar interactions are of minor importance for the PEG-lipid micelles compared to the repulsive forces from the steric interaction from the overlap of PEG layers) arose from the fact that all their experiments were made in 150 mM NaCl solutions. To clarify this aspect, we plan to investigate further the effect of ionic strength of solvent on the repulsive interactions of DSPE-PEG micelles. From the methodological point of view, the DRS/SAXS approach will be applicable to detailed physicochemical analyses of PEG-conjugated proteins, such as PEG-Hb and PEG-albumin.[44]

4. Conclusions

We have carried out SAXS and DRS experiments on aqueous solutions of PEG-conjugated phospholipid (DSPE-PEG) with

different M_{PEG} = 2000, 5000, and 12 000 Da. The results have provided deep physical insights into hydration and static structures of the DSPE-PEG micelles. The complex dielectric spectra of these solutions exhibit typical multistep relaxation behavior, the three relaxation processes centered at ~0.1, ~5, and ~19 GHz, being respectively assigned to the charged DSPE head group rotation, cooperative molecular motions in hydrated PEG layers, and cooperative hydrogen-bond network rearrangement dynamics of bulk water. A quantitative analysis of the bulk-water amplitude based on Cavell theory yields the effective hydration number of a DSPE-PEG molecule, $Z_{hyd} \sim 5.0$ (per ethylene oxide monomer unit), which turns out to be virtually independent of M_{PEG}. Although the extracted Z_{hyd} for DSPE-PEG, exceeding that for normal PEG by ca. 20%, involves inseparable effects of the DSPE charged head group hydration and packing of PEG chains into micellar structure, the finding clearly indicates that the hydration of PEG chains is mainly governed by the hydration of each EG monomer. In view of the pair-distance distribution functions, $p(r)$, deduced by the GIFT evaluation of the SAXS intensity distributions, the DSPE-PEGs produce nearly spherical micelles in aqueous environment, whose maximum diameters are estimated to be ~16, 22, and 31 nm, respectively, for M_{PEG} = 2000, 5000, and 12 000. The volume of DSPE-PEG and hydrated water molecules only accounts for 30−40% of the total micellar volume; the remaining more than 60% is occupied by bulk-like water. The structure factor $S(q)$ analysis unambiguously demonstrates that, at low ionic strength, both electrostatic repulsion induced by the charged head group and excluded volume effects of the hydrated PEG layer, significantly contribute to the net repulsive interaction among the PEG-lipid micelles, which should be a key factor for the function of PEG-lipids as a stabilizer of liposomes. Our finding does not necessarily support the generally accepted view that only the latter, excluded volume effect of hydrated PEG chains, is of major importance for the repulsive forces acting on PEG-lipid micelles. This will hold only at high ionic strength.

Acknowledgment. This work was supported in part by Health Sciences Research Grants (Research on Regulatory Science of Pharmaceuticals and Medical Devices), from the Ministry of Health, Labour, and Welfare, Japan, and Grants-in-Aid for Young Scientists (B) (No. 18740264) from the Ministry of Education, Culture, Sports, Science, and Technology (MEXT), Japan. T.S. acknowledges supports from the 21st century COE program at Waseda University funded by MEXT. The authors thank Alexander Stoppa for providing interferometer data of DSPE-PEG and PEG solutions. Professor Kenji Aramaki and late Professor Hironobu Kunieda are gratefully appreciated for their kind help for SAXS measurements. Some of the PEG-derivatives were kindly provided by NOF Co.

References and Notes

(1) Chandler, D. *Nature* **2005**, *437*, 640.
(2) Bangham, A. D.; Horne, R. W. *J. Mol. Biol.* **1964**, *12*, 660.
(3) Torchilin, V. P. *Nat. Rev. Drug Discovery* **2005**, *4*, 145.
(4) Klibanov, A. L.; Maruyama, K.; Torchilin, V. P.; Huang, L. *FEBS Lett.* **1990**, *268*, 235.
(5) Yoshioka, H. *Biomaterials* **1991**, *12*, 861.
(6) Mobed, M.; Chang, T. M. S. *Biomaterials* **1998**, *19*, 1167.
(7) Tsuchida, E., Ed. *Blood Substitutes, Present and Future Perspectives*; Elsevier Science S.A.: Lausanne, Switzerland, 1998.
(8) Sakai, H.; Tomiyama, K. I.; Sou, K.; Takeoka, S.; Tsuchida, E. *Bioconjugate Chem.* **2000**, *11*, 425.
(9) Sou, K.; Endo, T.; Takeoka, S.; Tsuchida, E. *Bioconjugate Chem.* **2000**, *11*, 372.
(10) Sakai, H.; Tsai, A. G.; Kerger, H.; Park, S. I. Takeoka, S.; Nishide, H.; Tsuchida, E.; Intaglietta, M. *J. Biomed. Mater. Res.* **1998**, *40*, 66.
(11) Sakai, H.; Takeoka, S.; Park, S. I.; Kose, T.; Nishide, H.; Izumi, Y.; Yoshizu, A.; Kobayashi, K.; Tsuchida, E. *Bioconjugate Chem.* **1997**, *8*, 23.
(12) Sou, K.; Klipper, R.; Goins, B.; Tsuchida, E.; Phillips, W. T. *J. Pharmacol. Exp. Ther.* **2005**, *312*, 702.
(13) Kenworthy, A. K.; Hristova, K.; Needham, D.; McIntosh, T. J. *Biophys. J.* **1995**, *68*, 1921.
(14) Johnsson, M.; Hansson, P.; Edwards, K. *J. Phys. Chem. B* **2001**, *105*, 8420.
(15) Koynova, R.; Tenchov, B.; Rapp, G. *Colloids Surf., A* **1999**, *149*, 571.
(16) Buchner, R.; Barthel, J. *Annu. Rep. Prog. Chem., Sect. C: Phys. Chem.* **2001**, *97*, 349.
(17) Fukasawa, T.; Sato, T.; Watanabe, J.; Hama, Y.; Kunz, W.; Buchner, R. *Phys. Rev. Lett.* **2005**, *95*, 197802.
(18) Sato, T.; Buchner, R. *J. Phys. Chem. A* **2004**, *108*, 5007.
(19) Sato, T.; Buchner, R. *J. Chem. Phys.* **2003**, *119*, 10789.
(20) Schrödle, S.; Hefter, G.; Kunz, W.; Buchner, R. *Langmuir* **2006**, *22*, 924.
(21) Sato, T.; Hossain, M. d. K.; Acharya, D. P.; Glatter, O.; Chiba, A.; Kunieda, H. *J. Phys. Chem. B* **2004**, *108*, 12927.
(22) Shikata, T.; Takahashi, R.; Sakamoto, A. *J. Phys. Chem. B* **2006**, *110*, 8941.
(23) Fernandez, P.; Schrödle, S.; Buchner, R.; Kunz, W. *ChemPhysChem* **2003**, *4*, 1065.
(24) Kaatze, U.; Gopel, K.-D.; Pottel, R. *J. Phys. Chem.* **1985**, *89*, 2565.
(25) Barthel, J.; Hetzenauer, H.; Buchner, R. *Ber. Bunsen Ges.* **1992**, *96*, 1424.
(26) Barthel, J.; Bachhuber, K.; Buchner, R.; Hetzenauer, H.; Kleebauer, K. *Ber. Bunsen Ges.* **1991**, *95*, 853.
(27) Glatter, O.; Kratky, O. *Small-Angle X-ray Scattering*; Academic: London, 1982.
(28) Lindner, P.; Zemb, Th., Eds. *Neutron, X-Ray and Light Scattering*; North-Holland: Amsterdam, 1991.
(29) Glatter, O. *J. Appl. Crystallogr.* **1997**, *10*, 415.
(30) Strey, R.; Glatter, O.; Schubert, K. -V.; Kaler, E. W. *J. Chem. Phys.* **1996**, *105*, 1175.
(31) Shrestha, L. K.; Sato, T.; Acharya D. P.; Iwanaga, T.; Aramaki, K.; Kunieda, H. *J. Phys. Chem. B* **2006**, *110*, 12266.
(32) Brunner-Popela, J.; Glatter, O. *J. Appl. Crystallogr.* **1997**, *30*, 431.
(33) Weyerich, B.; Brunner-Popela, J.; Glatter, O. *J. Appl. Crystallogr.* **1999**, *32*, 197.
(34) Orthaber, D.; Bergmann, A.; Glatter, O. *J. Appl. Crystallogr.* **2000**, *33*, 218.
(35) Bergmann, A.; Orthaber, D.; Scherf, G.; Glatter, O. *J. Appl. Crystallogr.* **2000**, *33*, 869.
(36) Fritz, G.; Bergmann, A.; Glatter, O. *J. Chem. Phys.* **2000**, *113*, 9733.
(37) Nilsson, P. G.; Lindman, B. *J. Phys. Chem.* **1983**, *87*, 4756.
(38) Hayter, J. B.; Penfold, J. *Mol. Phys.* **1981**, *42*, 109.
(39) Ornstein, L. S.; Zernike, F. *Proc. Sect. Sci. K. Ned. Akad. Wet.* **1914**, *17*, 793.
(40) Rogers, F. J.; Young, D. A. *Phys. Rev. A* **1984**, *30*, 999.
(41) Percus, J. K.; Yevick, G. J. *Phys. Rev.* **1958**, *110*, 1.
(42) Nagle, J. F.; Tristram-Nagle, S. *Biochim. Biophys. Acta* **2000**, *1469*, 159.
(43) Nagarajan, R.; Ruckenstein, E. *Langmuir* **1991**, *7*, 2934.
(44) Manjula, B. N.; Tsai, A.; Upadhya, R.; Perumalsamy, K.; Smith, P. K.; Malavalli, A.; Vandegriff, K.; Winslow, R. M.; Intaglietta, M.; Prabhakaran, M.; Friedman, J. M.; Acharya, A. S. *Bioconjugate Chem.* **2003**, *14*, 464.

Hemoglobin vesicles reduce hypoxia-related inflammation in critically ischemic hamster flap tissue

Jan A. Plock, MD; Annemarie E. Tromp, MD; Claudio Contaldo, MD; Timo Spanholtz, MD; Dubravko Sinovcic, MD; Hiromi Sakai, PhD; Eishun Tsuchida, PhD; Michael Leunig, MD; Andrej Banic, MD, PhD; Dominique Erni, MD

Objectives: **The aim of this study was to investigate the effect of a highly viscous, left-shifted hemoglobin vesicle solution (HbV) on the hypoxia-related inflammation and the microcirculation in critically ischemic peripheral tissue.**

Design: **Randomized prospective study.**

Setting: **University laboratory.**

Subjects: **Twenty-four male golden Syrian hamsters.**

Interventions: **Island flaps were dissected from the back skin of anesthetized hamsters for assessment with intravital microscopy. The flap included a critically ischemic, hypoxic area that was perfused via a collateralized vasculature. One hour after completion of the preparation, the animals received an injection of 25% of total blood volume of 0.9% NaCl or NaCl suspended with HbVs at a concentration of 5 g/dL (HbV5) or 10 g/dL (HbV10).**

Measurements and Main Results: **Plasma viscosity was increased from 1.32 cP to 1.61 cP and 2.14 cP after the administration of HbV5 and HbV10, respectively (both $p < .01$). Both HbV solutions raised partial oxygen tension (Clark-type microprobes) in the ischemic tissue from approximately 10 torr to 17 torr ($p < .01$), which was paralleled by an increase in capillary perfusion by >200% ($p < .01$). The 50% increase in macromolecular capillary leakage found over time in the control animals was completely abolished by the HbV solutions ($p < .01$), which was accompanied by a >50% ($p < .01$) reduction in cells immunohistochemically stained for tumor necrosis factor-α and interleukin-6 and in leukocyte counts, whereas no such changes were observed in the anatomically perfused, normoxic tissue.**

Conclusions: **Our study suggests that in critically ischemic, hypoxic peripheral tissue, hypoxia-related inflammation may be reduced by a top-load infusion of HbV solutions. We attributed this effect to a restoration of tissue oxygenation and an increase in plasma viscosity, both of which may have resulted in attenuation of secondary microcirculatory impairments. (Crit Care Med 2007; 35:899–905)**

KEY WORDS: blood substitutes; capillary hemodynamics; capillary leakage; tumor necrosis factor-α; interleukin-6; collateral circulation

In tissues rendered ischemic due to traumatic devascularization or arterial occlusion, hypoxia may occur when the vascular oxygen supply is no longer sufficient to cover the demand of adenosine triphosphate required to maintain normal physiologic function. Besides having a direct impact on cellular function and survival, hypoxia may induce an inflammatory response, thus causing secondary damage to the critically ischemic tissue.

Hypoxic inflammation is mediated by the activation of a large number of genes (1). In this scenario, a pivotal role has been ascribed to master regulators of hypoxic signaling, such as the hypoxia-inducible factor (HIF)-1α and nuclear factor-κB (1, 2). HIF-1α accumulates under hypoxic conditions due to the attenuation of its natural degradation, which takes place under normoxic conditions at a posttranscriptional level. In addition, HIF-1α induces the recruitment, adhesion, infiltration, and activation of leukocytes (3, 4). Target genes for nuclear factor-κB include the hyperacute proinflammatory cytokine tumor necrosis factor (TNF)-α (5) and the subacute proinflammatory cytokine interleukin (IL)-6 (6).

The primary approach to prevent hypoxic inflammation should be to correct the oxygen debt in the ischemic tissues. Improving vascular oxygen supply was the rationale for developing artificial oxygen carriers such as perfluorocarbons and modified hemoglobins (7, 8). In a previous series of experiments we were able to demonstrate that oxygenation and survival in collateralized, critically ischemic hamster flap tissue were improved after isovolemic hemodilution with colloidal solutions supplemented with phospholipid vesicles containing isolated, purified human hemoglobin (hemoglobin vesicles, HbVs) (9–12). Hemodilution, as well as the high viscosity and high colloid osmotic pressure of the HbV solutions, was responsible for the ben-

From the Department of Orthopedic, Plastic and Hand Surgery, Inselspital University Hospital, Berne, Switzerland (JP, AT, TS, DS, ML, AB and DE); Department of Reconstructive Surgery, University Hospital, Zurich, Switzerland (CC); and Advanced Research Institute for Science and Engineering, Waseda University, Tokyo, Japan (HS, ET).

Supported, in part, by grants 32-054092.98 and 32-065149.01 (DE) and grant 32–050771.97 (ML) from the Swiss National Foundation for Scientific Research; the Department of Clinical Research, University of Berne, Switzerland; Health Sciences Research (Research on Regulatory Science, H18-IYAKU-Ippan-021, 022) from the Ministry of Health, Labour and Welfare, Japan (HS, ET); Grants in Aid for Scientific Research from the Japan Society for the Promotion of Science (B16300162, HS); and Oxygenix Inc.

Drs. Sakai and Tsuchida are consultants for Oxygenix, Inc., own stock and stock options in the company, and hold patents related to technologies to produce Hb vesicles. The remaining authors have not disclosed any potential conflicts of interest.

DOI: 10.1097/01.CCM.0000257463.71761.97

eficial effect on the perfusion of the collateralized, ischemic microvasculature (9, 11, 12). Furthermore, our results suggested that the large size and high oxygen affinity of the HbVs caused a downstream shift of oxygen release toward the ischemic, collateralized tissue due to retention of oxygen in the upstream vasculature, which was correlated with the amount of circulating HbVs (10, 11).

The purpose of this study was to test whether the infusion of left-shifted HbV may attenuate hypoxia-induced inflammation in the well-established hamster flap model. Unlike previous experiments, HbVs were applied with a top-load infusion instead of an isovolemic blood exchange, and they were given without colloidal solutions. Both of these changes may be advantageous in a clinical setting due to the simplified mode of application and reduced risk of adverse effects. Because of their crucial role in critical ischemia, emphasis was put on the assessment of capillary hemodynamics. TNF-α and IL-6 concentrations and leukocyte accumulation in the critically ischemic tissue were taken as end points expressing inflammation.

MATERIALS AND METHODS

Animals and Solutions. Experiments were performed according to the National Institutes of Health guidelines for the care and use of laboratory animals and with the approval of the local Animal Ethics Committee. Twenty-four Syrian golden hamsters (Charles River, Sulzfeld, Germany) weighing 78–85 g were included in this study. The animals were randomly assigned and equally distributed to the sham-operated control group and three test groups receiving an infusion of either NaCl 0.9% or HbV suspended in NaCl at concentrations of 5 g/dL (HbV5) or 10 g/dL (HbV10). HbV was prepared as described previously (13). The physicochemical characteristics of the solutions are described in Table 1.

Animal and Flap Preparation. A hamster skin flap model was used as previously described in detail (9, 10, 14). Anesthesia was induced by pentobarbital injected intraperitoneally (100 mg/kg of body weight; Nembutal, Abbott Laboratories, Chicago, IL). The carotid artery and external jugular vein were cannulated for administration of anesthesia, infusion of the solutions, laboratory analysis, and monitoring of arterial blood pressure (Type514, Spacelabs, Hillsboro, OR). An island flap measuring 3 × 2 cm was dissected from the back skin of the animal. The flap consisted of skin and a thin layer of panniculus carnosus muscle and was perfused by one vascular axis that bifurcated into two equal-sized branches within the flap, each of them supplying a separate vascular territory. One of the branches was transected, thus rendering the corresponding vascular territory ischemic. This tissue was perfused by a collateral vasculature connecting the two vascular networks.

Laboratory Analysis. Blood samples were taken from the carotid artery catheter and collected in heparin-washed microtubes for immediate measurements of total hemoglobin concentration, pH, and systemic arterial Po_2 and Pco_2 (ABL 625; Radiometer, Copenhagen, Denmark). The colloid osmotic pressure of the diluents was measured with a colloid osmometer (4420, Wescor, Logan, UT) with a 30,000-D cutoff membrane. The viscosity of the solutions, blood, and plasma with and without HbVs was measured with a Höppler-type viscosimeter (HAAKE Messtechnik, Karlsruhe, Germany) at 25°C.

Microhemodynamics and Partial Tissue Oxygen Tension. Investigations were performed using an intravital microscope (Axioplan 1, Zeiss, Jena, Germany). Microscopic images were captured by a television camera (Intensified CCD camera, Kappa Messtechnik, Gleichen, Germany), recorded on video (50 Hz, Panasonic, Osaka, Japan), and displayed on a television screen (Trinitron PVM-1454QM, Sony, Tokyo, Japan). The preparation was observed visually with a ×40 objective with a numerical aperture of 0.75, which results in a theoretical resolution of approximately 300 nm and a total optical magnification of ×909 on the video monitor, where one pixel corresponded to 264 nm in the tissue. The microvessels were classified according to physiologic and anatomical features into conduit arterioles (connections to each other), end arterioles, and small venules (14, 15). The vessels were chosen for examination according to their optical clarity. The intraluminal microvascular diameters were measured visually on the television screen with the use of 2% fluorescein isothiocyanate-labeled dextran (molecular mass 150 kD; Sigma Chemical, Buchs, Switzerland) injected intra-arterially (0.05 mL), an excitation filter (485–505 nm), a dichroic mirror (510 nm), and a barrier filter (530 nm). The capillary hemodynamics and macromolecular leakage were assessed with a computer-assisted image analysis system (CapImage, Zeintl Software, Heidelberg, Germany) (12). Capillary diameters were obtained from the averages of five consecutive measurements. Because the capillary diameters measured with the present technique may possibly be underestimated due to the use of fluorescence microscopy and the optical properties of the microscope (16), the values were given in percentages of the mean obtained in the anatomically perfused tissue of the control group at baseline. Functional capillary density (FCD) was defined as the length of red blood cell (RBC)-perfused capillaries per observation field and expressed in cm/cm^2. The product of RBC velocity and FCD was taken as an index reflecting the perfusion of the tissue with RBCs. The endothelial integrity was assessed by measuring macromolecular leakage (17). This was achieved by densitometric analysis of the fluorescence of fluorescein isothiocyanate-labeled dextran 10 mins after its injection. Macromolecular leakage was expressed by the ratio of fluorescence obtained in the interstitial space vs. capillary and postcapillary venular fluorescence.

Tissue Po_2 was assessed with Clark-type microprobes consisting of polarographic electrodes inside of an oxygen-sensitive microcell (Revoxode CC1, GMS, Kiel, Germany). According to the manufacturer, the sampling area of the probes was within 1 mm of the microcell. The probes were inserted into the subcutaneous tissue in the center of each vascular territory under microscopic control. Care was taken to place the probes away from large arterioles and venules.

Immunohistochemistry. Tissue samples were obtained from the middle of each vascular territory at the end of the experiment. They were fixed in 4% paraformaldehyde, washed in phosphate-buffered saline, stored in 70% ethanol, and finally embedded in paraffin blocks. Five-micrometer sections were cut, transferred to microslides, and air-dried at 37°C overnight. Giemsa-staining was used for staining and identifying leukocytes. The counts included both endoluminal and migrated leukocytes. Additional sections were immunohistochemically stained for TNF-α and IL-6 after being treated with microwaves and incubated. The specimens were exposed to anti-TNF-α and anti-IL-6 antibodies (Sigma Chemical, Buchs, Switzerland). The biotin-conjugated anti-rabbit immunoglobulin G (Sigma Chemical, Buchs, Switzerland) served as the secondary antibody. The avidin-biotin peroxidase complex (DAKO, Glostrup,

Table 1. Physicochemical characteristics of hamster blood and diluents before and after top-load infusion

	Hamster Blood	Hamster Plasma	NaCl	HbV5	HbV10
[Hb], g/dL	18	0	0	5	10
Oncotic pressure, mm Hg		18	0	0	0
Viscosity of solution, cP		1.2	0.9	1.7	4.1
P50, torr	28			9	9
Plasma viscosity 4 hrs after infusion, cP		1.32 ± 0.03	1.30 ± 0.01	1.61 ± 0.02[a]	2.14 ± 0.10[a]

HbV5, HbV10, hemoglobin vesicles suspended in NaCl at Hb concentrations of 5 g/dL and 10 g/dL, respectively; [Hb], hemoglobin concentration.

[a] $p < .01$ vs. hamster plasma. Viscosity of the solutions and plasma was measured at 25°C.

Denmark), dimethylformamide (Fluka Chemicals, Buchs, Switzerland), and 3-amino-9-ethylcarbazole (Sigma Chemical, Buchs, Switzerland) were used for staining. Finally, the slides were slightly counterstained with Mayer's hematoxylin. Immunostaining was assessed semiquantitatively using a light microscope (Leica DM/RB, Leica, Wetzlar, Germany). All counts were performed in three randomly selected visual fields obtained at ×200 magnification. False-positive immunohistochemical staining was observed in hair follicles and sebaceous glands, which were therefore excluded from the semiquantitative analysis.

Protocol. The animals were kept under light anesthesia with a continuous infusion of 50 mg/mL pentobarbital given at a rate of approximately 0.5 $mg \cdot min^{-1} \cdot kg$ of body $weight^{-1}$ throughout the experiment. The depth of anesthesia was regulated by tolerating a noxious reflex due to pinching of the hind paw but no nonaversive reflexes (palpebral, corneal, and jaw reflex) (14). A heating pad was applied, and the room temperature was set at 28°C to keep the animal's abdominal skin temperature constant at 32°C.

Baseline measurements were taken after a postoperative stabilization period of 1 hr had elapsed. Thereafter, 25% of total blood volume of NaCl, HbV5, or HbV10 was infused over 15 mins. Exclusion criteria were abnormalities of the vascular anatomy, insufficient optical clarity, mean arterial pressure <60 torr, and systemic arterial pH, Po_2, and Pco_2 values out of the normal ranges at baseline (7.30–7.45, 35–55 torr, and 45–65 torr, respectively). The animals were killed with an overdose of pentobarbital at the end of the experiment after the tissue samples had been harvested.

Statistical Analysis. The InStat version 3.0 program (Graph Pad Software, San Diego, CA) was used for statistical analysis. The data are presented as mean ± SD. The time-related differences between repeat measurements were assessed by paired analysis of variance, followed by the Dunnett's posttest. Differences between the groups were assessed by unpaired analysis of variance and Tukey's posttest. A value of $p < .05$ was taken to represent statistical significance.

Table 2. Systemic and laboratory data at baseline and 1 and 4 hrs after top-load infusion

	Baseline	1 Hr	4 Hrs
MAP, mm Hg			
Control	108 ± 6	103 ± 8	100 ± 5
NaCl	103 ± 6	102 ± 5	100 ± 4
HbV5	102 ± 2	104 ± 3	103 ± 2
HbV10	102 ± 5	104 ± 8	100 ± 3
Total Hb concentration, g/dL			
Control	17.8 ± 1.0	17.6 ± 1.1	17.3 ± 1.1
NaCl	17.9 ± 0.7	17.3 ± 0.7	16.1 ± 1.0[a]
HbV5	17.2 ± 1.0	16.8 ± 1.0	15.2 ± 0.6[a]
HbV10	18.2 ± 0.7	18.2 ± 0.6	17.3 ± 0.5[a]
Po_2, torr			
Control	49 ± 10	51 ± 9	53 ± 7
NaCl	50 ± 4	56 ± 9	60 ± 10
HbV5	44 ± 4	45 ± 5	56 ± 12
HbV10	46 ± 7	46 ± 7	57 ± 10[b]
Pco_2, torr			
Control	51 ± 5	50 ± 5	48 ± 3
NaCl	53 ± 4	47 ± 7	43 ± 6[b]
HbV5	58 ± 5	56 ± 4	49 ± 9[b]
HbV10	53 ± 4	47 ± 7	46 ± 9
pH			
Control	7.32 ± 0.03	7.31 ± 0.06	7.28 ± 0.04
NaCl	7.34 ± 0.03	7.34 ± 0.05	7.33 ± 0.04
HbV5	7.30 ± 0.06	7.30 ± 0.02	7.33 ± 0.06
HbV10	7.32 ± 0.04	7.33 ± 0.04	7.32 ± 0.06

HbV5, HbV10, hemoglobin vesicles suspended in NaCl at hemoglobin concentrations of 5 g/dL and 10 g/dL, respectively.

[a]$p < .01$, [b]$p < .05$ vs. baseline.

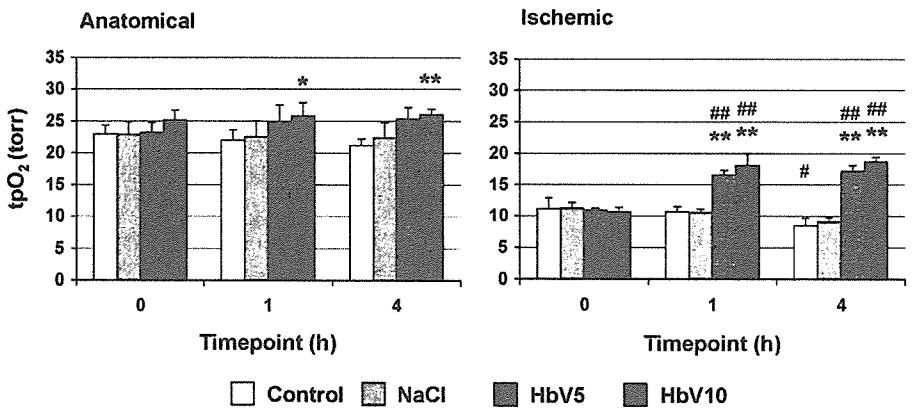

Figure 1. Partial oxygen tension (ptO_2) in the anatomically perfused and ischemic tissues at baseline and after top-load infusion of 0.9% NaCl, and hemoglobin vesicles suspended in NaCl at hemoglobin concentrations of 5 g/dL (*HbV5*) and 10 g/dL (*HbV10*). Data represent mean values and SD. #$p < .05$, ##$p < .01$ vs. baseline; *$p < .05$, **$p < .01$ vs. control.

RESULTS

Three animals (one control, one NaCl, and one HbV5) did not fulfill the inclusion criteria and were excluded from this study.

The systemic data are presented in Table 2. Mean arterial pressure remained virtually unchanged over time in all groups. Mean Hb concentrations ranged between 17.2 g/dL and 18.2 g/dL at baseline, which corresponded to hematocrits of ~55%. Hb concentration was reduced by ~10% 4 hrs after administration of NaCl and HbV5 and ~5% after HbV10 (all $p < .01$). The infusions increased mean Po_2 from 44–50 torr to 56–60 torr (not significant for NaCl and HbV5, $p < .05$ for HbV10). Plasma viscosity was raised to 1.61 cP after HbV5 and 2.14 cP after HbV10 (both $p < .01$ vs. control) but not after NaCl (Table 1).

Oxygen tension was significantly reduced in the ischemic tissue compared with the anatomically perfused part ($p < .01$, Fig. 1). The animals receiving HbV solutions revealed a Po_2 increase from ~11 torr to 17.1 torr (HbV5) and 18.7 torr (HbV10) in the ischemic tissue (both $p < .01$ vs. baseline and control).

The baseline microvascular diameters were ~40 μm for conduit arterioles, ~10 μm for end arterioles, and ~90 μm for venules. The values were similar in all groups and in both parts of the flap, and they remained virtually unchanged throughout the experiments.

The behavior of the capillary hemodynamics is shown in Figure 2. At baseline, the capillaries in the ischemic tissue were significantly wider than the anatomically perfused capillaries (overall means of 4.46 μm vs. 4.06 μm, $p < .01$). In the

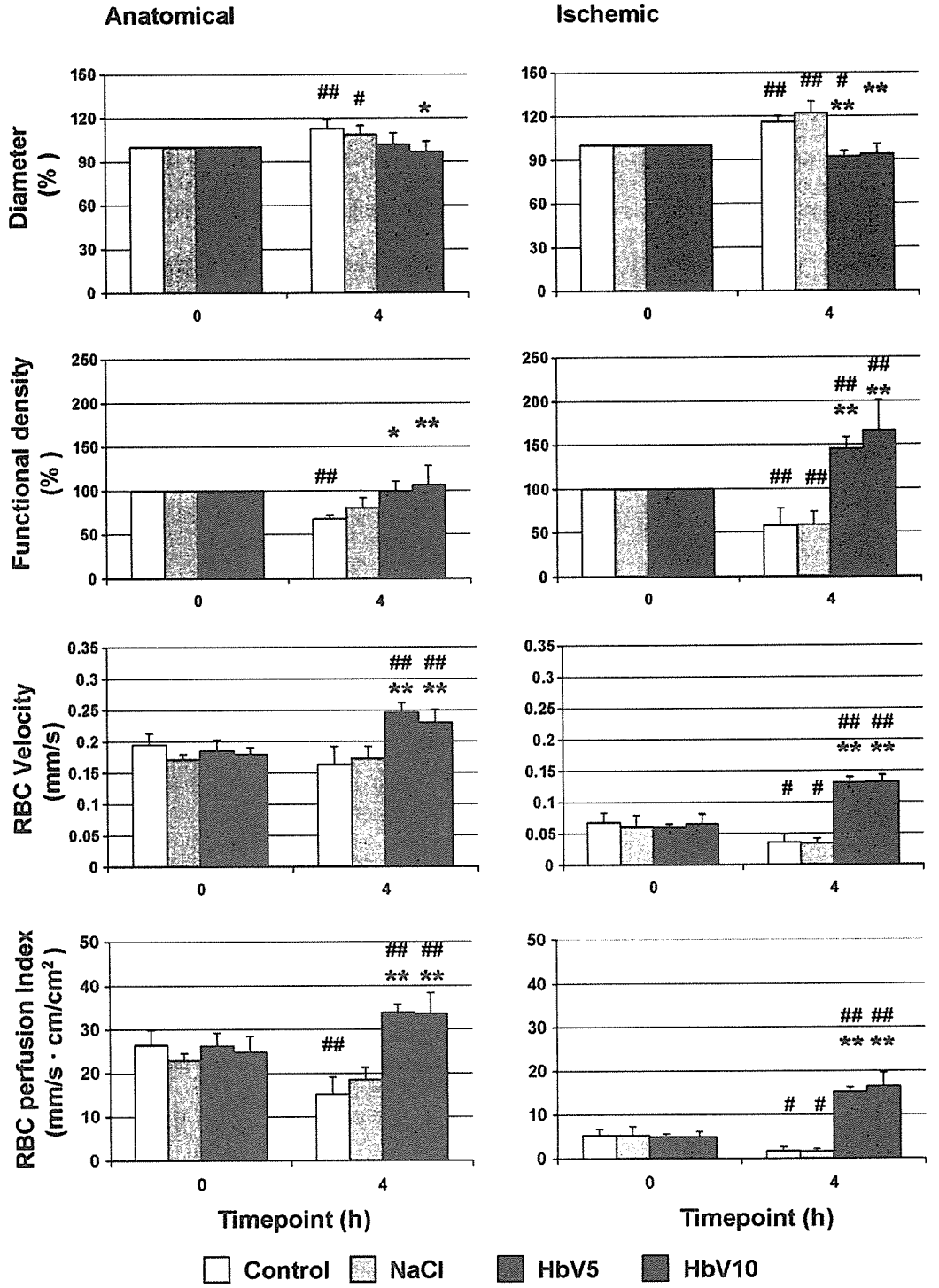

Figure 2. Capillary hemodynamics in the anatomically perfused and ischemic tissues at baseline and after top-load infusion of 0.9% NaCl, and hemoglobin vesicles suspended in NaCl at hemoglobin concentrations of 5 g/dL (*HbV5*) and 10 g/dL (*HbV10*). Data represent mean values and SD. The values for capillary diameter and functional capillary density were expressed in percentage of baseline. #$p < .05$, ##$p < .01$ vs. baseline; *$p < .05$, **$p < .01$ vs. control. *RBC*, red blood cell.

control group, the capillaries further dilated over time in both the anatomically perfused and the ischemic tissues by 13% and 16%, respectively (both $p < .01$). This time-related dilation was significantly attenuated by HbV ($p < .01$). The induction of ischemia reduced baseline FCD by ~40% ($p < .01$). In the control group, FCD, RBC velocity, and the calculated RBC perfusion index further decreased over time ($p < .05$ for ischemic). Both HbV solutions kept FCD at baseline levels in the anatomically perfused part ($p < .05$ vs. control) and increased FCD in the ischemic tissue by 45% after HbV5 and 66% after HbV10 (both $p < .01$ vs. baseline and control). RBC velocity was increased by ~30% in the anatomically perfused tissue and ~120% in the ischemic tissue (both $p < .01$ vs. baseline and control), and the RBC perfusion index was increased by ~30% in the anatomically perfused tissue and by >200% in the ischemic tissue (all $p < .01$ vs. base-